Monthly Notices of the ROYAL ASTRONOMICAL SOCIETY

MNRAS **532,** 4729–4751 (2024) https://doi.org/10.1093/mnras/stae1732
Advance Access publication 2024 July 17

LeMMINGs. Multiwavelength constraints on the co-existence of nuclear star clusters and AGN in nucleated galaxies

B. T. Dullo [1,2★] J. H. Knapen,[3,4] R. D. Baldi [5,6] D. R. A. Williams [7] R. J. Beswick,[7] I. M. McHardy,[6] D. A. Green [8] A. Gil de Paz,[2,9] S. Aalto,[10] A. Alberdi,[11] M. K. Argo [12] J. S. Gallagher,[13] H.-R. Klöckner,[14] J. M. Marcaide,[15] I. M. Mutie [7,16] D. J. Saikia [17] P. Saikia,[18] I. R. Stevens [19] and S. Torrejón[2]

Affiliations are listed at the end of the paper

Accepted 2024 July 12. Received 2024 July 5; in original form 2023 July 14

ABSTRACT

The relation between nuclear star clusters (NSCs) and the growth of the central supermassive black holes (SMBHs), as well as their connection to the properties of the host galaxies, is crucial for understanding the evolution of galaxies. Recent observations have revealed that about 10 per cent of nucleated galaxies host hybrid nuclei, consisting of both NSCs and accreting SMBHs that power active galactic nuclei (AGNs). Motivated by the potential of the recently published multiwavelength data sets from LeMMINGs survey, here we present the most thorough investigation to date of the incidence of hybrid nuclei in a large sample of 100 nearby nucleated galaxies (10 E, 25 S0, 63 S, and 2 Irr), covering a wide range in stellar mass ($M_{*,\rm gal} \sim 10^{8.7} - 10^{12}$ M$_\odot$). We identify the nuclei and derive their properties by performing detailed 1D and 2D multicomponent decompositions of the optical and near-infrared *HST* stellar light distributions of the galaxies using Sérsic and core-Sérsic models. Our AGN diagnostics are based on homogeneously derived nuclear 1.5 GHz *e*-MERLIN radio, *Chandra* X-ray (0.3–10 keV), and optical emission-line data. We determine the nucleation fraction ($f_{\rm nuc}$) as the relative incidence of nuclei across the LeMMINGs *HST* sample and find $f_{\rm nuc} =$ 100/149 (= 67 ± 7 per cent), confirming previous work, with a peak value of 49/56 (= 88 ± 13 per cent) at bulge masses $M_{*,\rm bulge} \sim 10^{9.4} - 10^{10.8}$ M$_\odot$. We identify 30 nucleated LeMMINGs galaxies that are optically active, radio-detected, and X-ray luminous ($L_{\rm X} > 10^{39}$ erg s^{-1}). This indicates that our nucleated sample has a lower limit ∼ 30 per cent occupancy of hybrid nuclei, which is a function of $M_{*,\rm bulge}$ and $M_{*,\rm gal}$. We find that hybrid nuclei have a number density of (1.5 ± 0.4) × 10^{-5} Mpc^{-3}, are more common at $M_{*,\rm gal} \sim 10^{10.6} - 10^{11.8}$ M$_\odot$ and occur, at least, three times more frequently than previously reported.

Key words: galaxies: elliptical and lenticular, cD – galaxies: fundamental parameters – galaxies: nuclei – galaxies: photometry – galaxies: structure – radio continuum: galaxies.

1 INTRODUCTION

Central massive objects appear to be ubiquitous at the centres of galaxies, and may be a supermassive black hole (SMBH, with mass $M_{\rm BH} \sim 10^5 - 10^{10}$ M$_\odot$), a dense stellar nucleus or a combination of both. All nearby galaxies with stellar masses ($M_{*,\rm gal}$) above 10^{10} M$_\odot$ are thought to host a SMBH at their centre (Magorrian et al. 1998; Richstone et al. 1998; Ferrarese & Ford 2005; Kormendy & Ho 2013; Graham 2016). Conversely, at the lower stellar masses ($M_{*,\rm gal} \sim 10^8 - 10^{10}$ M$_\odot$) evidence for dynamically identified SMBHs is scarce and nuclear star clusters (NSCs) are routinely observed. NSCs are compact, typically having half-light radii of a few parsecs and stellar masses in the range $M_{*,\rm NSC} \sim 10^5 - 10^8$ M$_\odot$ (e.g. Böker et al. 2004; Côté et al. 2006). *Hubble Space Telescope (HST)* observations have revealed that as much as ∼80 per cent of galaxies of low and intermediate stellar masses host a dense stellar nucleus at their centres (Phillips et al. 1996; Böker et al. 2002; Graham & Guzmán 2003; Böker et al. 2004; Scarlata et al. 2004; Côté et al. 2006; Balcells, Graham & Peletier 2007; Georgiev & Böker 2014). We use the term 'nucleated' when referring to galaxies that possess nuclei, which are bright and compact optical sources at or near the galaxies' photocenters (Côté et al. 2006; Dullo & Graham 2012; Dullo, Martínez-Lombilla & Knapen 2016). The fraction of nucleated galaxies has been reported to increase systematically with galaxy stellar mass, reaching a peak at $M_{*,\rm gal} \sim 10^{9.5}$ M$_\odot$ before decreasing at higher galaxy masses (e.g. den Brok et al. 2014; Sánchez-Janssen et al. 2019; Neumayer, Seth & Böker 2020; Hoyer et al. 2021; Zanatta et al. 2021; Román et al. 2023).

SMBH and NSC masses have been shown independently to scale with several host galaxy properties, including luminosity, stellar mass, and central velocity dispersion (e.g. Carollo et al. 1997; Carollo, Stiavelli & Mack 1998; Ferrarese et al. 2006b; Neumayer et al. 2020, references therein). The coexistence of NSCs and SMBHs powering the AGN may therefore suggest that their formation is coupled and they grow concurrently regulated by the

★ E-mail: bdullo@ucm.es

same physical process (Seth et al. 2008; Antonini, Barausse & Silk 2015). Theoretical models predict NSCs promote the formation and growth of intermediate-mass BHs (IMBHs) and SMBHs (Gnedin, Ostriker & Tremaine 2014; Antonini et al. 2015; Stone, Küpper & Ostriker 2017; Kroupa et al. 2020; Askar, Davies & Church 2021; Baldassare et al. 2022) and facilitate accretion on to the central SMBH by funnelling gas towards the innermost regions (Naiman et al. 2015).

An outstanding question is how commonly accreting SMBHs powering AGN and dense stellar nuclei coexist at the centre of galaxies, and whether this occurrence is connected to the mass of the host galaxy. It has been suggested (e.g. Ferrarese et al. 2006b; Wehner & Harris 2006), in general, massive galaxies only contain non-stellar nuclei (SMBHs) whereas low mass galaxies contain compact stellar nuclei. In fact only ~ 20 per cent of core-Sérsic galaxies, which are massive ($M_{*,\rm gal} \gtrsim 10^{11}$ M$_\odot$) with depleted stellar cores, host stellar nuclei (Côté et al. 2006; Dullo & Graham 2012; Turner et al. 2012; Dullo & Graham 2013, 2014; den Brok et al. 2014; Dullo, Graham & Knapen 2017; Spengler et al. 2017; Dullo 2019). Bekki & Graham (2010), Antonini et al. (2015), and Antonini, Gieles & Gualandris (2019) hypothesized that the low incidence of NSCs in core-Sérsic galaxies is due to their tidal destruction post dynamical heating by coalescing binary SMBHs during gas-poor galaxy mergers.

However, an increasing number of galaxies, including the Milky Way, are found to host nuclei consisting of both a stellar nucleus and an AGN or a quiescent SMBH (e.g. González Delgado et al. 2008; Seth et al. 2008; Graham & Spitler 2009; Gallo et al. 2010; Leigh, Böker & Knigge 2012; Neumayer & Walcher 2012; Kormendy & Ho 2013; Georgiev & Böker 2014; Antonini et al. 2015; Foord et al. 2017; Nguyen et al. 2018). The Milky Way itself contains a SMBH of mass $\sim 4 \times 10^6$ M$_\odot$ (Ghez et al. 1998; Gillessen et al. 2009; Event Horizon Telescope Collaboration 2022) and a NSC with a mass $\sim (2.1 - 4.2) \times 10^7$ M$_\odot$ (Feldmeier et al. 2014; Schödel et al. 2014; Neumayer et al. 2020). While the current technological limitations hinder dynamical BH mass measurements at lower masses (Greene & Ho 2004; Reines et al. 2011), the mass range for hosting hybrid (NSC+AGN) nuclei also include low-mass galaxies (e.g. Nguyen et al. 2018; Yang et al. 2023). AGNs have been increasingly discovered in these systems, primarily with X-ray observations, albeit at a low AGN fraction rate of $\sim 1 - 5$ per cent (e.g. Gallo et al. 2010; Sartori et al. 2015; Mezcua et al. 2018; Penny et al. 2018; Birchall, Watson & Aird 2020; Dullo et al. 2023a, b). A well-known low-mass ($M_{*,\rm gal} \sim 3.4 \times 10^7$ M$_\odot$; Graham & Spitler 2009) galaxy which hosts a hybrid nucleus is NGC 4395 (Filippenko & Sargent 1989; Filippenko & Ho 2003; den Brok et al. 2015; Nandi et al. 2023). It is a bulgeless SA(s)m with a type 1 Seyfert nucleus. Other low-mass, hybrid nuclei host candidates are Pox 52, a dwarf elliptical galaxy (e.g. Barth et al. 2004; Thornton et al. 2008), and the dwarf disc galaxy RGG 118 (Baldassare et al. 2017).

Both NSCs and AGN emit radiation across the entire electromagnetic spectrum from radio to X-ray. Radio emission in NSCs is predominately driven by thermal stellar processes (e.g. Smith et al. 2020), whereas active SMBHs are associated with non-thermal processes driven by disc/corona winds or (sub-)relativistic jets (Panessa et al. 2019). Distinguishing between a spatially resolved, 'pure' NSC, a 'pure' AGN (unresolved), and any combination of the two in optical images is challenging. Nevertheless, they can all be included in a sample of 'nucleated' galaxies constructed from *HST* imaging. To differentiate them and determine the distinct origin of their nuclear emission, multiband diagnostics are necessary.

Previous studies have reported that the fraction of hybrid nuclei in (nucleated) galaxies is $\sim$10 per cent (e.g. Seth et al. 2008; Gallo et al. 2010; Foord et al. 2017). The useful work by Seth et al. (2008) investigated the presence of AGN in a sample of 176 previously reported galaxies with NSCs using radio, X-ray, and optical spectroscopic observations. Of their 75 galaxies with available optical spectral data, seven (10 per cent) host an optical AGN, whereas an additional 11 (15 per cent) exhibit composite, i.e. AGN-(star formation)-like emission. To detect radio emission, they used the very large array (VLA) Faint Images of the Radio Sky at Twenty cm (FIRST; Becker, White & Helfand 1995) at 1.4 GHz, with a sensitivity limit of 1.0 mJy and resolution of 5 arcsec. While 13 galaxies had radio detections within 30 arcsec of the NSCs, none of them were found to host AGN. Using heterogeneous X-ray data from *Chandra*, *ROSAT*, and XMM–Newton X-ray data, they identified 22 X-ray sources associated with their NSCs, and concluded 4/22 sources were likely AGN. Gallo et al. (2010) examined the AGN activity in 100 early-type Virgo galaxies (Côté et al. 2006) using *Chandra* observations, finding a hybrid nucleus fraction of 0.3–7 per cent for $M_{*,\rm gal} < 10^{11}$ M$_\odot$. Antonini et al. (2015) used semi-analytical models and found that the fraction of galaxies with a hybrid nucleus increases from $\sim$5 per cent at $M_{*,\rm gal} \sim 10^9$ M$_\odot$ to 30 per cent at $M_{*,\rm gal} \sim 10^{12}$ M$_\odot$. Recently, Foord et al. (2017) used *Chandra* X-ray observations and found that $\sim$11.2 per cent of their sample of 98 galaxies with NSCs harbour hybrid nuclei.

The Legacy *e*-MERLIN Multiband Imaging of Nearby Galaxies Survey (LeMMINGs; Beswick et al. 2014; Baldi et al. 2018, 2021a, b) aims to investigate the underlying physical mechanisms that drive nuclear emission in galaxies by combining high resolution observations from radio (*e*-MERLIN), through optical (*Hubble Space Telescope, HST*) to X-ray (*Chandra*). In this work, we use the results from our 1D and 2D multicomponent *HST* imaging analysis to accurately identify the nuclei in LeMMINGs galaxies and derive their properties (Dullo et al. 2023b). For a robust characterization of the coexistence of NSCs and AGN, our AGN diagnostics rely on homogeneously obtained 1.5 GHz *e*-MERLIN radio observations of nuclei with a sub-mJy sensitivity and resolution of $\sim$0.15 arcsec, as well as nuclear *Chandra* X-ray and optical emission-line data from LeMMINGs (Baldi et al. 2018, 2021a; Williams et al. 2022). The sample covers a wide range in stellar mass, morphology, and nuclear activity, which are crucial to establish the scaling relations between the mass and luminosity of the nuclei and their radio and X-ray luminosities.

This study constitutes the most comprehensive multiwavelength investigation to date of the connection between NSCs and AGN in nearby galaxies. The paper is organized as follows. Section 2 provides a description of the radio and optical emission-line data and discusses the 1D and 2D multicomponent decompositions with *HST* imaging that were used to characterize the nuclei. In Section 3, we present the relation between nucleation fraction and several properties, including the luminosity, stellar mass of the host galaxy and its bulge, and Hubble type. Also discussed in this section is the co-existence of NSCs and AGN in LeMMINGs galaxies. Section 4 presents scaling relations between the mass/luminosity of nuclei and their radio and X-ray luminosities and discusses the implications. Finally, we summarize in Section 5. There are four appendices at the end of this paper (Appendices A1–A4). Our 2D decompositions and comparison with previous fits in the literature are given in Appendices A1 and A2, respectively. The global and central properties of the sample galaxies are given in Appendix A3, while Appendix A4 provides a comparison between our censored (ASURV) and uncensored (BCES bisector) regression fits for the full sample of nuclei.

Table 1. Multiwavelength data.

Data	*N* Parent sample/this work
(1)	(2)
1.5 GHz *e*-MERLIN radio data[1r]	280/100
Optical spectral classification[1r]	280/100
Chandra X-ray (0.3–10 keV) data[2r]	213/84
HST 1D data[3r]	173/173
HST 2D nucleated galaxy data[3r]	42/42
HST 2D nucleated galaxy data (this work)	58/58

Note. (1): multiwavelength data used in this work. (2): number of galaxies (*N*) in the parent sample and in the subsample used in this work. The sample in this study consists of 100 nucleated galaxies. Of this, 42 had 2D decompositions of their *HST* images in Dullo et al. (2023b), while for the remaining 58, we performed 2D decompositions of the *HST* images here. References. 1r = Baldi et al. (2018, 2021a, b); 2r = Williams et al. (2022); 3r = Dullo et al. (2023b).

Throughout this paper, we use $H_0 = 70$ km s^{-1} Mpc^{-1}, $\Omega_m = 0.3$, and $\Omega_\Lambda = 0.7$ (e.g. Freedman et al. 2019), an average of the Planck 2018 Cosmology $H_0 = 67.4 \pm 0.5$ km s^{-1} Mpc^{-1} (Planck Collaboration VI 2020) and the LMC $H_0 = 74.22 \pm 1.82$ km s^{-1} Mpc^{-1}(Riess et al. 2019). All magnitudes are in the Vega system, unless specified otherwise.

2 DATA

In what follows, we will describe the optical, radio, and X-ray data which are used in the paper to study nucleation in LeMMINGs galaxies. Except for 58 per cent of the 2D decompositions of the *HST* images discussed here, all other data used in this work are published elsewhere (Baldi et al. 2018, 2021a, b; Williams et al. 2022; Dullo et al. 2023b).

2.1 Radio, X-ray data, and optical spectral classification

The LeMMINGs (Beswick et al. 2014; Baldi et al. 2018, 2021a, b; Williams et al. 2023) is a survey of 280 nearby galaxies, above declination $\delta > +20^\circ$, see Tables 1 and 2. The sample is a subset of the magnitude-limited ($B_T \leq 12.5$ mag and declinations $\delta > 0^\circ$) Palomar spectroscopic sample of 486 bright, nearby galaxies (Ho, Filippenko & Sargent 1995, 1997a), which in turn were drawn from the Revised Shapley-Ames Catalogue of Bright Galaxies (Sandage & Tammann 1981) and the Second Reference Catalogue of Bright Galaxies (de Vaucouleurs, de Vaucouleurs & Corwin 1976). The LeMMINGs declination cutoff is implemented to ensure optimal radio visibility coverage for the *e*-MERLIN array. The primary goal of the survey is to provide the deepest high-resolution radio continuum study of the local Universe at a sub-mJy sensitivity of $\sim$ 0.08 mJy beam^{-1} and an angular resolution of $\sim$ 0.15 arcsec. The 1.5 GHz radio continuum of the 280 galaxies were observed with *e*-MERLIN for a total of 810 h (Baldi et al. 2018, 2021a). The radio detection and radio core luminosities for our sample are tabulated in Table A2.

Williams et al. (2022) analysed *Chandra* X-ray observations of the nuclei of a sample of 213 LeMMINGs galaxies. Of the 100 nucleated LeMMINGs galaxies targeted in this study, 84 have *Chandra* X-ray data. With an angular resolution of 0.5 arcsec and a flux limit of 1.65×10^{-14} erg s^{-1} cm^{-2} at 0.3–10 keV, the authors detected X-ray emission in 150/213 galaxies, coincident within 2 arcsec of the optical nucleus.

We use the optical spectral classes from Baldi et al. (2018, 2021a), who presented updated spectral classifications using emission-line ratios taken mainly from Ho, Filippenko & Sargent (1997a, see also Filippenko & Sargent 1985; Ho et al. 1995, 1997a; Ho et al. 1997b; Ho et al. 1997c). Baldi et al. (2018, 2021a) also used new emission-line ratio data from recent observations to refine the spectral classification for some sample galaxies. They applied the emission line diagnostic diagrams by Kewley et al. (2006) and Buttiglione et al. (2010). Baldi et al. (2018, 2021a) categorized the galaxies with nuclear emission lines as Seyfert, LINER, and H II galaxies, whereas LeMMINGs galaxies that lack nuclear emission lines were referred to us 'absorption line galaxies (ALGs)'.

In this paper, the galaxies referred to as 'optically active' (i.e. AGN) are LINERs and Seyferts, while those referred to as 'radio AGN' are, following Baldi et al. (2018), jetted objects with radio morphologies B ('one-sided jet'), C ('triple'), and D ('doubled-lobed') as well as radio detected LINERs and Seyferts lacking detected jets with *e*-MERLIN at 1.5 GHz.

2.2 Sample selection and identification of nuclei with *HST*

One of the aims of this paper is a detailed investigation of the structural properties of photometrically distinct nuclei observed in the broad-band *HST* images of nearby galaxies, paying particular attention to NSCs and AGN (see Table 1). We define nuclei as distinct central light excesses with respect to the inward extrapolation of outer Sérsic or core-Sérsic models which are fitted to the underlying bulge[1] profiles or to the outer disc profiles for bulgeless galaxies (e.g. Côté et al. 2006; Dullo & Graham 2012; Turner et al. 2012; Dullo et al. 2016; Dullo et al. 2019). NSCs are compact with half-light radii ($R_{\rm e,nuc}$) as small as a few parsecs (e.g. Böker et al. 2004; Côté et al. 2006) and for the most extended ones $R_{\rm e,nuc} \sim 1$ arcsec (e.g. Turner et al. 2012). The identification of nuclei depends strongly on the resolution of the imaging used, high-resolution *HST* data being most suitable. At the mean distance of our nearby sample galaxies ($D \sim 22$ Mpc), the *HST* (ACS, WFPC2, WFC3, and NICMOS) angular resolution of 0.05–0.1 arcsec corresponds to $\sim$ 5−10 pc. Identification of a nucleus and robust measurements of its luminosity/stellar mass and effective radius also requires detailed photometric decomposition of the host galaxy's stellar light distribution. It is essential to account for the effects of the PSF to reliably separate the central light excess from the rest of the galaxy. In Dullo et al. (2023b), we revealed that the bulge mass can be significantly overestimated when galaxy components such as bars, rings, and spirals are not included in the fits. This implies that restricting fits to bulge–disc profiles can yield inaccurate structural parameters for the nuclei.

Dullo et al. (2023b) used *HST* (ACS, WFPC2, WFC3, and NICMOS) images and extracted surface brightness profiles for 173 LeMMINGs galaxies (23 E, 42 S0, 102 S, and 6 Irr), see Table 1. In that study, we performed accurate, 1D multicomponent decompositions of the surface brightness profiles covering a large radial extent of $R \gtrsim 80 - 100$ arcsec ($\gtrsim 2R_{\rm e,bulge}$), fitting up to six galaxy components (i.e. bulge, disc, partially depleted core, nuclei, bar, spiral arm, and stellar halo and ring), simultaneously, using Sérsic model (Sérsic 1963, 1968) $R^{1/n}$ and core-Sérsic model (Graham et al. 2003; Trujillo et al. 2004; Ferrarese et al. 2006a; Baldi

[1]The term 'bulge' is traditionally associated with the spheroidal component of disc galaxies but it is used here to refer to the underlying host spheroid in case of elliptical galaxies and the bulge for S0, spiral, and irregular galaxies.

Table 2. Optical and radio properties.

Galaxies (1)	Number (per centage) (full *HST* sample/nucleated) (2)	Radio-detected fraction (full *HST* sample/nucleated) (3)
E	23 (13.2 per cent)/10 (10 per cent)	11/23 (47.8 per cent)/3/10 (30.0 per cent)
S0	42 (24.3 per cent)/25 (25 per cent)	25/42 (59.5 per cent)/15/25 (60.0 per cent)
S	102 (59.0 per cent)/63 (63 per cent)	47/102 (46.0 per cent)/32/63 (50.8 per cent)
Irr	6 (3.5 per cent)/2 (2 per cent)	2/6 (33.3 per cent)/0/2 (0.0 per cent)
Seyfert	10 (5.8 per cent)/9 (9 per cent)	8/10 (80.0 per cent)/7/9 (77.8 per cent)
ALG	23 (13.3 per cent)/9 (9 per cent)	5/23 (21.7 per cent)/1/9 (11.1 per cent)
LINER	71 (41 per cent)/48 (48 per cent)	49/71 (69.0 per cent)/30/48 (62.5 per cent)
H II	69 (39.9 per cent)/34 (34 per cent)	21/69 (30.4 per cent)/12/34 (35.3 per cent)
Total	173 (100 per cent)/100 (100 per cent)	83/173 (48.0 per cent)/50/100 (50.0 per cent)

Note. The sample galaxies are first separated based on the galaxy morphological and optical spectral classes (1–2) and then further divided based on their radio detection (3), see Section 2.1. The term 'full *HST* sample' refers to the sample of 173 LeMMINGs galaxies with *HST* data (Dullo et al. 2023b), see Table 1.

et al. 2010; Dullo & Graham 2012; Dullo 2019). To decompose a galaxy light profile in 1D, we convolved the individual fitted components with a Gaussian point-spread function (PSF) in 2D.

We note that the parent LeMMINGs sample of 280 galaxies constitute all the Palomar galaxies (Ho et al. 1995, 1997a) with $\delta > 20^{\circ}$. As the Palomar sample is statistically complete, it implies that the parent LeMMINGs sample is also statistically complete. As shown by Dullo et al. (2023b, see their figs 1 and 3 and the discussion in Section 2), the *HST* sample of 173 LeMMINGs galaxies is representative of the parent LeMMINGs sample of 280 galaxies, and therefore is not expected to be biased in terms of nucleation and nuclear activity (see Tables 1 and 2).

The 1D decompositions presented in Dullo et al. (2023b) identified nucleation in 124/173 galaxies. In that analysis, we revealed that a two-parameter Gaussian function (i.e. a special case of the Sérsic model when $n = 0.5$) describes the light profile of 94/124 nuclei, while we fit a three-parameter Sérsic model with $0.4 \lesssim n \lesssim 2.5$ and a median $n \sim 0.7 \pm 0.6$ to describe the light profiles for the remaining 30 nuclei. From this initial sample of 124 nuclei, we have excluded 24 that do not allow reliable determination of the NSC structural parameters because their central source is either too large or too small, see Section 2.4 for further discussion. In what follows, we focus primarily on the remaining sample of 100 (= 124−24) nucleated LeMMINGs galaxies (10 E, 25 S0, 62 S, and 3 Irr).

As mentioned above, the identification of the 100 nuclei is based on detailed 1D and 2D decompositions of the host galaxies' stellar light distributions from the broad-band *HST* data (Table 1). To classify the nuclei as either dense star clusters, 'pure' AGN, or a combination of both, we use multiwavelength AGN diagnostics that rely on homogeneously derived, nuclear 1.5 GHz *e*-MERLIN radio, *Chandra* X-ray (0.3–10 keV), and optical emission-line data (Section 3).

2.3 1D and 2D multicomponent decomposition

Fig. 1 shows the 1D multicomponent decompositions of the major-axis surface brightness profiles for a dozen nucleated LeMMINGs galaxies. The galaxies were selected to be representative examples for the 100 nucleated galaxies in terms of morphology and number of fitted galaxy structural components. Of these 12 galaxies, images of NGC 147, NGC 221, NGC 959, and NGC 2500 were obtained with *HST* in the WFPC2 F814W filter, whereas those for NGC 3756, NGC 3982, NGC 4750, NGC 4800, and NGC 6951 were obtained with the *HST* ACS F814W filter. For the remaining three objects, we used *HST* data from the WFPC2 in the following filters: F547M (NGC 3884), F791W (NGC 4151), and F606W (NGC 4449).

Dullo et al. (2023b) performed 2D decompositions of the *HST* images for 65/173 galaxies (Table 1). These 2D fits had the same type and number of galaxy structural components as the corresponding 1D fits. The 2D model images were convolved with a Moffat PSF generated using the IMFIT task MAKEIMAGE. Our findings suggested that detailed 1D and 2D decompositions yield strong agreements, regardless of the galaxy morphology under consideration. Of the 100 sample nucleated galaxies (Tables 1 and A2 and Section 2.4), 42 had 2D decompositions in Dullo et al. (2023b). Here, we follow their fitting methodology and perform 2D decompositions of the *HST* images for the remaining 58 nucleated galaxies using IMFIT V.1.8 (Erwin 2015), see Table A2. We note that of the 12 representative galaxies shown in Fig. 1, eight are among these 58 galaxies newly fitted in 2D, while the remaining four (NGC 959, NGC 3756, NGC 3884, and NGC 4449) had their 2D fits published in Dullo et al. (2023b).

Fig. 2 compares the 1D and 2D properties of the nuclei including the (a) central and effective surface brightnesses, i.e. $\mu_{0,\rm nuc}$ and $\mu_{\rm e,nuc}$, respectively, (b) effective radii, $R_{\rm e,nuc}$ and (c) Sérsic indices, $n_{\rm nuc}$. We note that the $\mu_{\rm e,nuc}$ and $n_{\rm nuc}$ values are only for the 21/100 galaxies whose nuclei were fitted with a Sérsic model. As in Dullo et al. (2023b), we find strong agreement between the 1D and 2D fits, where the $\mu_{0,\rm nuc}/\mu_{\rm e,nuc}$, $R_{\rm e,nuc}$, and $n_{\rm nuc}$ values from the two methods are within the 1σ error ranges for 89, 87, and 62 per cent of the cases. For 97, 92, and 76 per cent of the cases, the 1D versus 2D measurements of $\mu_{0,\rm nuc}/\mu_{\rm e,nuc}$, $R_{\rm e,nuc}$, and $n_{\rm nuc}$, respectively, are within 2σ of perfect agreement. Marginal discrepancies between 1D and 2D measurements are expected, as these two methods inherently differ from each other. We follow Turner et al. (2012) and Dullo et al. (2023b) and adopt the results from our 1D decompositions in this work. In Appendix A2, we compare our data, fitting methods, and sample with those from the literature, to explain improvements and discrepancies when they exist.

Apparent magnitudes of the nuclei are determined by integrating the best-fitting Sérsic and Gaussian profiles to $R = \infty$. We applied foreground Galactic extinction corrections to the magnitudes using the reddening values from Schlafly & Finkbeiner (2011). For S0, spiral, and irregular galaxies, we additionally correct for internal dust attenuation using equations from Driver et al. (2008). We applied the same amount of internal dust correction to the nuclei and their host bulge. The internal dust corrections, the transformation of magnitudes from various *HST* filters into V-band magnitudes are

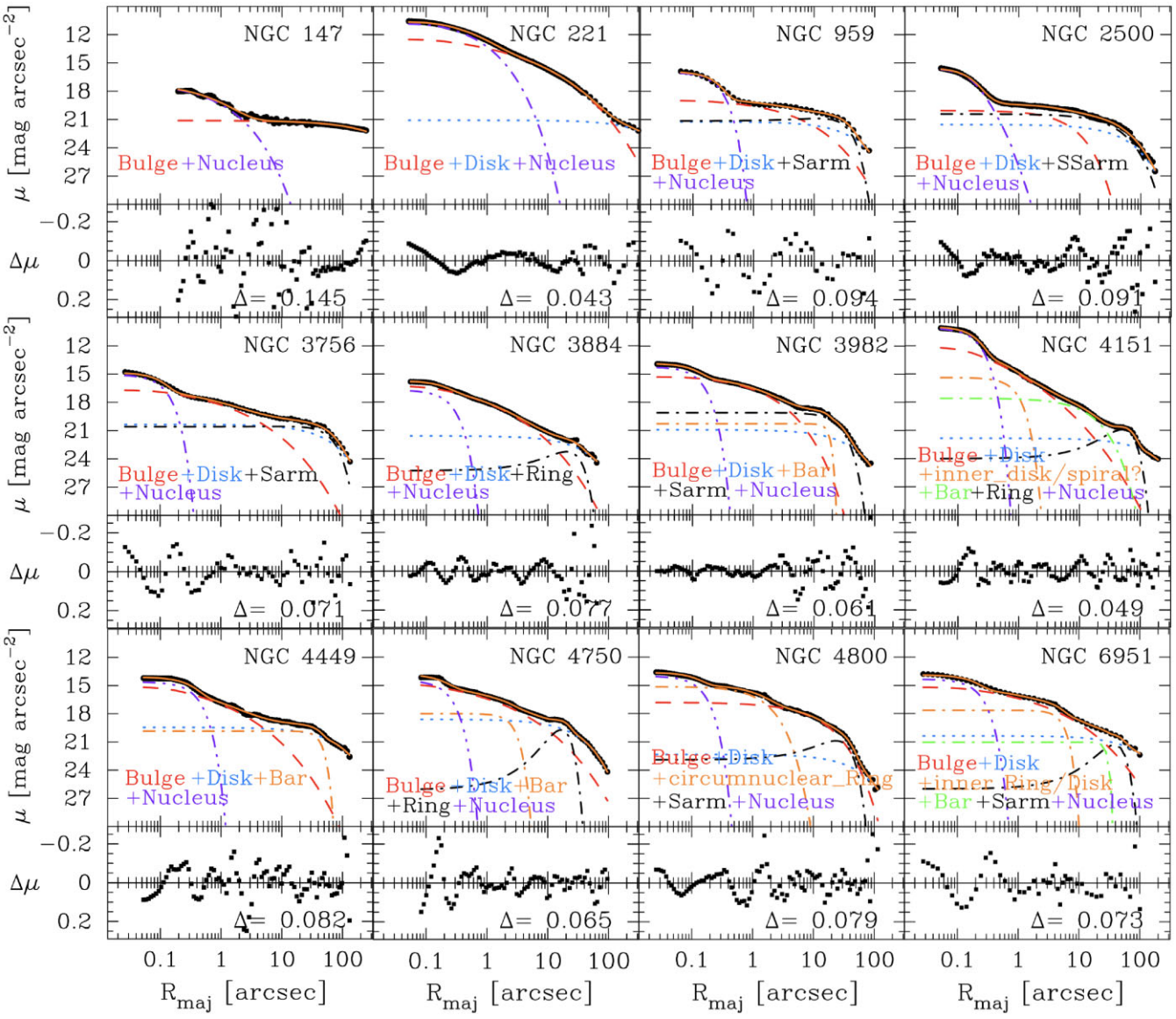

Figure 1. 1D multicomponent decompositions of the major-axis surface brightness profiles for a dozen nucleated LeMMINGs galaxies, selected as representative examples from the 100 nucleated galaxies in our sample (Table A2; Dullo et al. 2023b). The residual profiles along with the rms residual (Δ) for each fit are shown. While the images for NGC 147, NGC 221, NGC 959, and NGC 2500 were observed with *HST* in the WFPC2 F814W filter, those for NGC 3756, NGC 3982, NGC 4750, NGC 4800, and NGC 6951 were obtained with the *HST* ACS F814W filter. For the remaining three the *HST* images are from the WFPC2 and obtained in the following filters: NGC 3884 (F547M), NGC 4151 (WF791W), and NGC 4449 (F606W). The magnitudes are given in the Vega magnitude system. We fitted the nuclei typically with a two-parameter Gaussian model (dash-dot-dot-dot purple curve), while for some galaxies, the nuclei were described using a Sérsic model (dash-dotted purple curve). The dashed red (Sérsic) curves represent the bulges, while the dotted blue curve shows the large-scale discs which we modelled with an exponential function. Galaxy components such as bars and small-scale discs, rings, spirals, and lenses are described by Sérsic models (i.e. dash-dotted orange and green curves). Large-scale ring and spiral arm ('Sarm') components were fitted with three-parameter Gaussian ring models (dash-dotted black curve). For NGC 2500, the galaxy's spiral-arm was described using a Sérsic model ('SSarm'). The complete fits (solid orange curves) match the observed galaxy profiles with a median rms residual $\Delta \sim 0.065$ mag arcsec^{-2}. We fit up to six model components which are summed up to a full model with up to 16 free parameters.

discussed in Dullo et al. (2023b, their section 3.3). After correcting the nuclei magnitudes for dust, they were converted to stellar masses.

Table A2 presents the nucleus, bulge, and galaxy structural data for the 100 nucleated galaxies. We note that the full *HST* sample covers over six orders of magnitude in bulge stellar mass and contains all Hubble types from E to Im (Hubble 1926; de Vaucouleurs 1959), Tables 1, 2, and A2. Of the 100 nuclei, three are hosted by bulgeless, late-type galaxies (NGC 3077, NGC 4656, and NGC 5112). Table A3 presents the nucleus, bulge, and galaxy structural data for the 24 excluded LeMMINGs galaxies with nuclei.

2.4 Excluded nuclei

As previously noted, we use 1D and 2D decompositions and exclude 24 out of 124 nuclei in the sample, see Tables A2 and A3. Böker et al. (2004) reported a median half-light effective radius of 3.5 pc for their sample of 39 NSCs (see also Seth et al. 2006). Côté et al. (2006)

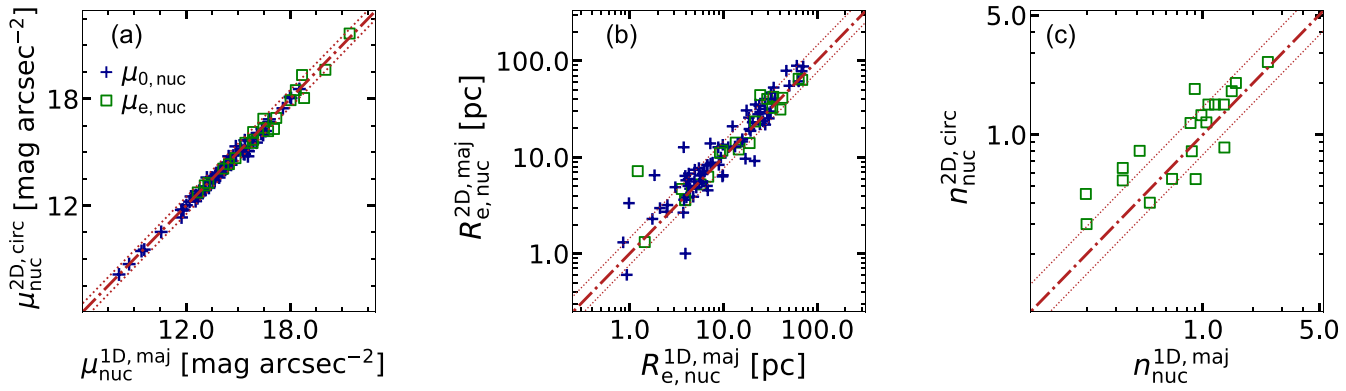

Figure 2. 2D versus 1D structural properties of nuclei from our multicomponent decompositions of the *HST* images for sample galaxies (Section 2.2, Table A2). Of the 100 nuclei in the sample, 79 were described using a Gaussian model (blue crosses), whereas the remaining 21 were fitted with a Sérsic model (green boxes). Comparison of 1D and 2D (a) central surface brightnesses of the nuclei ($\mu_{0,\rm nuc}$) or surface brightnesses of the nuclei at the effective radii $R_{\rm e}$ ($\mu_{\rm e,nuc}$), (b) major-axis effective radii of the nuclei ($R_{\rm e,nuc}$), and (c) Sérsic indices of the nuclei ($n_{\rm nuc}$). The dash-dotted lines are the one-to-one relations, while the dotted lines show the 1σ uncertainties.

reported half-light radii for NSCs which are $R_{\rm e,nuc} \sim 1-50$ pc (see also Böker et al. 2004), later work found NSCs with $R_{\rm e,nuc} \sim 1-80$ pc and stellar masses $M_{*,\rm nuc} \sim 10^5 - 10^9$ M$_\odot$ (Turner et al. 2012; den Brok et al. 2014; Georgiev et al. 2016).

Of the 24 excluded nuclei, 13 nuclei were too large for a NSC (+AGN), with extended half-light radii of $R_{\rm e,nuc} \gtrsim 80$ pc. In contrast, 9/24 nuclei have sizes $R_{\rm e,nuc} < 1$ pc, whereas the remaining 2/24 nuclei have low stellar masses of $M_{*,\rm nuc} < 10^5$ M$_\odot$. The hosts of the two low-mass nuclei (IC 2574 and NGC 5204) are optically inactive, with no detectable nuclear radio emission at 1.5 GHz by *e*-MERLIN (see Table A3). This suggests that these nuclei are not AGN, instead they may be globular clusters (e.g. Côté et al. 2006). Among the 9/24 nuclei where the structural analysis gives $R_{\rm e,nuc} < 1$ pc, one galaxy, NGC 3031, hosts a resolved nucleus ($R_{\rm e,nuc} \sim 0.14$ arcsec ~ 0.43 pc). The remaining eight were unresolved in the *HST* images ($R_{\rm e,nuc} << 0.05$ arcsec). For these eight galaxies we report upper-limit values of $R_{\rm e,nuc} = 0.05$ arcsec (Table A3) given the resolution limit in the *HST* images.

We consider the possibility that the nine nuclei with $R_{\rm e,nuc} <$ 1 pc are 'pure' AGN. Only three of them are hosted by optically active galaxies (NGC 3031, i.e. M81, NGC 3642, and NGC 5273). For NGC 3642 ($M_{*,\rm nuc} \sim 1.3 \times 10^7$ M$_\odot$) and NGC 5273 ($M_{*,\rm nuc} \sim 9.6 \times 10^7$ M$_\odot$), the nuclei, having effective radii of $R_{\rm e,nuc} \sim 0.002$ arcsec ~ 0.15 pc, are unresolved and deep within the *HST* PSF. As such, their structural properties are less secure, making it difficult to determine whether they are AGN and/or (bright) undersized NSCs. On the other hand, NGC 3031, which is detected both in the radio (Baldi et al. 2018, 2021a; $L_{\rm R,core,\ 1.5GHz} \sim 3.2 \times 10^{35}$ erg s^{-1}) and X-ray (Williams et al. 2022; $L_{\rm X} \sim 1.6 \times 10^{39}$ erg s^{-1}), hosts a compact nucleus with $R_{\rm e,nuc} \sim 0.14$ arcsec ~ 0.43 pc and $M_{*,\rm nuc} \sim 1.1 \times 10^6$ M$_\odot$. Our results from the multiband analyses seem to indicate the presence of a genuine compact AGN in NGC 3031. We defer the analysis of the two low-mass nuclei and the nine nuclei with $R_{\rm e,nuc} < 1$ pc to a future work and exclude them from our current sample.

Lastly, we explore the possibility that some nuclei in our final sample may be due to inner stellar discs. These inner discs tend to be more massive and extended compared to NSCs/AGN (e.g. Balcells et al. 2007; Dullo & Graham 2012). Fig. 3 compares the distribution of our major-axis effective radii for the nuclei with the distributions of circular effective radii of nuclei from the literature (Côté et al. 2006; Georgiev et al. 2016). While nine nuclei in the final sample have

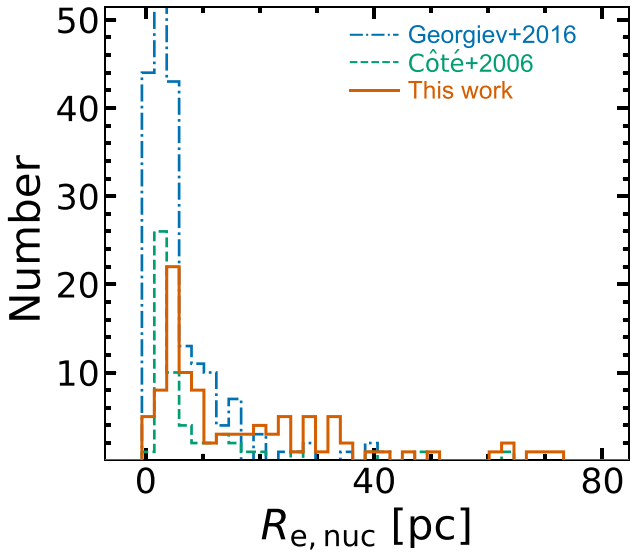

Figure 3. Comparison of the distribution of our 1D major-axis effective (half-light) radii of the nuclei (solid orange histogram) and previous circular effective radii of nuclei from Côté et al. (2006), dashed green histogram, and Georgiev et al. (2016), dash-dotted blue histogram.

masses $M_{*,\rm nuc} \sim 10^9 - 10^{10}$ M$_\odot$, we classify them as NSCs/AGN rather than extended inner discs because their effective radii are $R_{\rm e,nuc} \sim 10-70$ pc, with a mean value of ~ 38.5 pc, and they have low ellipticities ranging from 0.09 to 0.3, with a mean value of ~ 0.19 (see Fig. 3, Table A2). Furthermore, Georgiev et al. (2016) reported nuclei stellar masses of $M_{*,\rm nuc} \sim 10^5 - 10^9$ M$_\odot$. The median stellar mass for their 228 host galaxies with nuclei is $M_{*,\rm gal} \sim 4 \times 10^9$ M$_\odot$, approximately an order of magnitude smaller than the median stellar mass for our sample galaxies ($M_{*,\rm gal} \sim 5.3 \times 10^{10}$ M$_\odot$). Given that the stellar masses of the nuclei scale with the host galaxy stellar masses (e.g. Georgiev et al. 2016; Pechetti et al. 2020; Hoyer et al. 2023; Dullo, in preparation), the nine nuclei in our sample with $M_{*,\rm nuc} \sim 10^9 - 10^{10}$ M$_\odot$ are expected (see Turner et al. 2012). Finally, we note that the 100 nuclei in this study (Table A2) should not be confused with the extra central light components that were identified in Sérsic elliptical galaxies using hydrodynamical

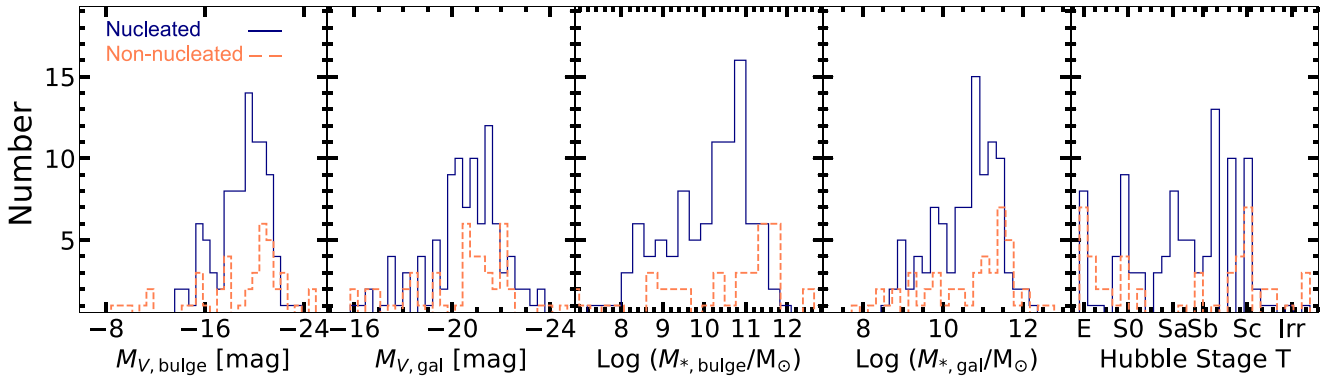

Figure 4. Distributions of $M_{V,\mathrm{bulge}}$, $M_{V,\mathrm{gal}}$, $M_{*,\mathrm{bulge}}$, $M_{*,\mathrm{gal}}$, and morphology for nucleated (blue histograms) and non-nucleated galaxies (orange histograms) in our sample of 149 galaxies with *HST* data. Our analysis excludes 24 galaxies with central light excesses, as explained in the text. Note that, including these 24 galaxies in the analysis does not significantly alter the observed trends.

Table 3. Galaxy property intervals.

Range	Galaxies per bin	Range	Galaxies per bin	Range	Galaxies per bin
(1)	(2)	(1)	(2)	(1)	(2)
$-M_{V,\mathrm{bulge}}$		log $M_{*,\mathrm{bulge}}$		Hubble type	
7.0–14.5	18	< 9.0	40	–5.0–(–4.0)	23
14.5–16.0	13	9.0–10.0	25	–3.6–0.5	34
16.0–18.0	21	10.0–10.5	24	0.6–4.0	43
18.0–19.0	13	10.5–11.0	27	4.0–7.0	39
19.0–20.0	28	11.0–11.5	22	7.0–9.0	10
20.0–21.0	27	11.5–12.5	11	–	–
21.0–24.0	29	–	–	–	–
$-M_{V,\mathrm{gal}}$		log $M_{*,\mathrm{gal}}$			
15.7–17.0	11	8.0–9.0	14	–	–
17.0–19.0	20	9.0–10.0	29	–	–
19.0–20.0	17	10.0–10.5	17	–	–
20.0–21.0	42	10.5–11.0	31	–	–
21.0–22.0	36	11.0–11.5	38	–	–
22.0–24.0	23	11.5–12.5	20	–	–

Note. In order to calculate the nucleation fraction (f_{nuc}), we split the sample into five to seven $M_{V,\mathrm{bulge}}$, $M_{V,\mathrm{gal}}$, $M_{*,\mathrm{bulge}}$, $M_{*,\mathrm{gal}}$, and Hubble type bins.

simulations (Hopkins et al. 2009, their fig. 45), see also Kormendy & Ho (2013). These latter components typically have an extended profile with an effective radius of 100–500 pc.

3 RESULTS

3.1 Nucleation fraction as a function of luminosity, stellar mass, and Hubble type

To investigate the relation between nucleation and host galaxy properties, in Fig. 4 we show the distributions of bulge absolute magnitude ($M_{V,\mathrm{bulge}}$), galaxy absolute magnitude ($M_{V,\mathrm{gal}}$), bulge stellar mass ($M_{*,\mathrm{bulge}}$), galaxy stellar mass ($M_{*,\mathrm{gal}}$), and Hubble type for the 100 nucleated (blue histograms) and 49(= 173−24 − 100) non-nucleated (orange histograms) LeMMINGs galaxies. We define the nucleation fraction f_{nuc} as the ratio between the number of nucleated galaxies and the total number of galaxies in the bin under consideration (Table 3). When calculating f_{nuc}, we *did not* take into account the 24 excluded LeMMINGs galaxies (Section 2.4). We calculate f_{nuc} for each bin of the absolute magnitude, stellar mass, and Hubble type distributions (see Table 3). In Fig. 5, we plot f_{nuc} against the mean $M_{V,\mathrm{bulge}}$, $M_{V,\mathrm{gal}}$, $M_{*,\mathrm{bulge}}$, $M_{*,\mathrm{gal}}$, and Hubble type values for each bin (Table 3). We find that f_{nuc} is a strong function of $M_{V,\mathrm{bulge}}$, $M_{V,\mathrm{gal}}$, $M_{*,\mathrm{bulge}}$, and $M_{*,\mathrm{gal}}$ (Figs 5a–d).

The nucleation fraction peaks at intermediate stellar mass and luminosity ranges, declining at faint and bright end of the luminosity function. Over the full absolute magnitude/mass range (Fig. 4), the nucleation fraction is f_{nuc} =100/149 (= 67 ± 7 per cent). Note that the errors quoted in this section are Poisson errors. If we treat the 24 excluded galaxies (Section 2.4) as non-nucleated then f_{nuc} =100/173 (= 58 ± 6 per cent) for the full LeMMINGs *HST* sample. The nucleation fraction has a peak value of 49/56 (= 88 ± 13 per cent), which occurs at bulge masses $M_{*,\mathrm{bulge}} \sim 10^{9.4} - 10^{10.8}$ M$_\odot$ (Fig. 5). We find that the trends of the nucleation fraction with the stellar mass and absolute magnitude of the host galaxy are reminiscent of the trends with those of the bulge.

The nucleation fraction across the LeMMINGs sample agrees very well with those reported in previous studies (typically $f_{\mathrm{nuc}} \sim 50 - 80$ per cent), which are summarized in Table A1 (Carollo et al. 1997; Carollo et al. 1998; Ravindranath et al. 2001; Stiavelli et al. 2001; Böker et al. 2002; Carollo et al. 2002; Balcells et al. 2003; Graham & Guzmán 2003; Lotz, Miller & Ferguson 2004; Grant et al. 2005; Lauer et al. 2005; Côté et al. 2006; Balcells et al. 2007; Turner et al. 2012; den Brok et al. 2014; Sánchez-Janssen et al. 2019; Seth, Neumayer & Böker 2020; Hoyer et al. 2021; Zanatta et al. 2021; Su et al. 2022). However, from visual inspections of ground-based images of dwarf galaxies located in low-to-moderate density environments, Poulain et al. (2021) reported a relatively low nucleation frequency of $f_{\mathrm{nuc}} \sim 23$ per cent. In comparison, Stiavelli et al. (2001) reported $f_{\mathrm{nuc}} \sim 56$ per cent for dwarf ellipticals (dEs) in the Virgo and Fornax Clusters and Leo group. Similarly, Graham & Guzmán (2003) and den Brok et al. (2014) reported $f_{\mathrm{nuc}} \sim 87$ and 80 per cent for dwarf galaxies in the Coma Cluster, respectively, whereas Grant et al. (2005) found $f_{\mathrm{nuc}} \sim 61$ per cent for dEs in the Virgo cluster.

We find that nuclei are less common in core-Sérsic galaxies, which instead exhibit a partially depleted core (Dullo & Graham 2014; Dullo et al. 2017; Dullo et al. 2018; Dullo 2019). This is in agreement with Bekki & Graham (2010) and Antonini et al. (2015) who suggested that coalescing SMBH binaries with individual mass of $M_{\mathrm{BH}} \gtrsim 10^8$ M$_\odot$ can heat and lower central stellar density, thus fully destroying the central NSC in core-Sérsic galaxies during gas-poor mergers. We have identified two nucleated core-Sérsic galaxies (NGC 3193 and NGC 4278) out of the 20 core-Sérsic

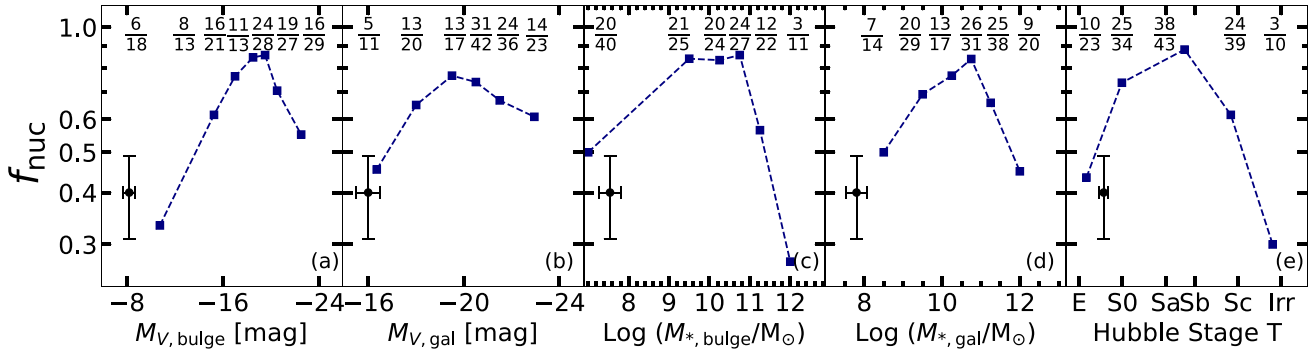

Figure 5. Nucleation fraction (f_{nuc}) as a function of (a) bulge V-band absolute magnitude $M_{V,bulge}$, (b) total V-band absolute galaxy magnitude $M_{V,gal}$, (c) bulge stellar mass $M_{*,bulge}$, (d) galaxy stellar mass $M_{*,gal}$, and (e) morphology. A representative error bar is shown at the bottom left of each panel.

Table 4. Types of nuclei.

Nuclei	Note	Sample	Radio jetted	X-ray data/detected
(1)	(2)	(3)	(4)	(5)
NSC	inactive (optical)	43	0	34/21
	radio-detected (30 per cent)	–	–	–
Hybrid	AGN (optical)	57	13	50/47
	radio-detected (65 per cent)	–	–	–

Note. We have classified the 100 nuclei in the sample into NSCs (43 per cent) and hybrid nuclei (57 per cent).

galaxies in LeMMINGs, i.e. $f_{nuc} = 10 \pm 7$ per cent. Combining our LeMMINGs data with the core-Sérsic data from our past work (Dullo & Graham 2014; Dullo 2019; Dullo et al. 2023b) yields a slightly higher nucleation fraction of 10/51(20 ± 6 per cent, see also Côté et al. (2006), Dullo & Graham (2012), Turner et al. (2012), den Brok et al. (2014), Spengler et al. (2017), and Dullo (2019). Conversely, nuclei are commonplace in Sérsic galaxies ($f_{nuc} = 98/129 = 76 \pm 8$ per cent).

When separated by the Hubble type, we find that the nucleation fractions for elliptical (Hubble $T < -4$), S0 ($-4 \leq T < 1$), and S ($1 \leq T < 9$) galaxies are 10/23 ($= 44 \pm 14$ per cent), 25/34 ($= 74 \pm 15$ per cent), and 63/87 ($= 72 \pm 9$ per cent), respectively. Nucleation was detected in 2/5 ($= 40 \pm 28$ per cent) of Irr galaxies, but this figure is not conclusive due to the small number statistics (e.g. Neumayer et al. 2020; Seth et al. 2020; Hoyer et al. 2021).

3.2 Characterization of nuclei

The sample under investigation consists of 100 nucleated galaxies. Using optical emission-line data, the nuclear activities of the galaxies were classified as either 'inactive', ALG+H II for 43 galaxies or 'active', Seyfert+LINER, for 57 galaxies (Baldi et al. 2018, 2021a), see also Section 2.1 and Tables 2 and 4. We checked for the presence of radio jets in the sample ALGs and H II galaxies from weakly active SMBHs. None of the ALGs and H II galaxies host radio jets that can be detected with *e*-MERLIN at 1.5 GHz.

3.2.1 NSCs

We classify the nuclei detected in the 43 inactive (i.e. 9 ALG + 34 H II) galaxies as 'pure' NSCs, where the bulk of the central light excess in the optical or near-IR brightness profiles of the galaxies is of stellar origin (Tables 2 and 4). Our *e*-MERLIN observations detected nuclear radio emission in thirteen of these 43 NSCs (30 per cent). We consider the possibility that the nuclei in the nine ALGs could be powered by non-stellar emission of low-level AGN. The nine ALGs all have $M_{*,bulge} < 10^{11}$ $M_\odot$ and include three dwarf satellites of M31, the Andromeda Galaxy (NGC 147, NGC 205, and NGC 221, e.g. Ibata et al. 2013). All, except for one of them (NGC 2634), lack radio detection with *e*-MERLIN at 1.5 GHz. Consequently, we cannot conclude that the nuclei in the 9 ALGs are mainly due to AGN. Note that high-sensitivity (sub-mJy) radio continuum observations with *e*-MERLIN enable detection of low-luminosity AGN at scales of a few tens of parsecs. Of the 43 'pure' NSC hosts in the sample, 34 have *Chandra* X-ray data from LeMMINGs and we find 21/34 (~ 62 per cent) are X-ray detected. The majority of these X-ray detected nuclei (13/21) have luminosities $L_X \lesssim 10^{39}$ erg s^{-1}, possibly indicating that the X-ray emission originate mainly from ULXs/XRBs (Williams et al. 2022). The eight remaining nuclei (i.e. 2 ALG + 6 H II) have $L_X > 10^{39}$ erg s^{-1}. While only 50 per cent of these bright nuclear X-ray sources have been radio detected with *e*-MERLIN, generating their core X-ray emission may require non-thermal sources such as a weak AGN as well as contributions from ULXs and XRBs. None the less, we classify all the 43 nuclei as 'pure' NSCs, in line with their optical spectral classifications.

3.2.2 Hybrid nuclei

We classify the nuclei identified in the 57 optically active, nucleated galaxies as 'hybrid = NSC+AGN' (Table 4). Of these 57 hybrid nuclei, 50 have *Chandra* X-ray data available from LeMMINGs (Williams et al. 2022), see Table 4. A vast majority of these sources (47/50) are X-ray detected, with 81 per cent of the X-ray detected, nucleated sources having X-ray luminosities $L_X \gtrsim 10^{39}$ erg s^{-1}. We also find a high radio-detection fraction for these active nucleated hosts, 37/57 (65 per cent). There are only three active galaxies with nuclei in the sample lacking detectable, nuclear radio, and X-ray emission (NGC 3486, NGC 4150, and NGC 4274, see Baldi et al. 2021a, b; Williams et al. 2022).

We extend our efforts to investigate hybrid nuclei within our sample that may have most of their optical/near-IR flux originating from the AGN, thus exhibiting behaviour closely resembling that of 'pure' AGN. Our motivation partly arises from the observation of massive (core-Sérsic) galaxies ($M_{*,bulge} \gtrsim 10^{11}$ $M_\odot$), hosting massive SMBHs ($M_{BH} \gtrsim 10^8$ $M_\odot$). These galaxies are less likely to contain NSCs, which are believed to be tidally disrupted by the inspiralling massive SMBH binary that form during galaxy mergers

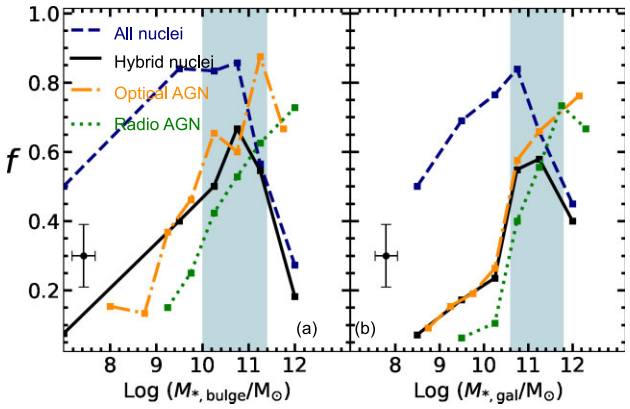

Figure 6. The trend between the fraction of hybrid (NSC+AGN) nuclei and the bulge and galaxy stellar mass (solid curves). The trends of optical and radio AGN fractions with $M_{*,bulge}$ and $M_{*,gal}$ (dash-dotted and dotted curves, respectively) are taken from Dullo et al. (2023a) and shown here for comparison. The identification of radio and optical AGN is based on the nuclear radio continuum emission and optical emission-line data (Section 2.1). The trend of all types of nuclei with $M_{*,bulge}$ and $M_{*,gal}$ (see Fig. 5) is also shown for comparison. We note that the fraction f for all types of nuclei is derived as the ratio between the number of nucleated galaxies and the total number of galaxies under consideration (Section 3.1). The fraction of galaxies hosting hybrid nuclei increases with $M_{*,bulge}$ and $M_{*,gal}$, peaking at intermediate masses ($M_{*,bulge}/M_{*,gal} \sim 10^{10.0} - 10^{11.4}$ M$_\odot$/$10^{10.6} - 10^{11.8}$ M$_\odot$) before decreasing at higher stellar masses. Representative error bars are shown at the bottom of the panels.

(Antonini et al. 2015; Antonini et al. 2019). Additionally, all our nucleated galaxies with $M_{*,bulge} \gtrsim 10^{11}$ M$_\odot$ are active.

Therefore, we focus on radio-detected core-Sérsic galaxies hosting hybrid nuclei, suggesting that a significant fraction of the optical/near-IR flux in these nuclei is likely generated by the AGN. It should be noted that the low-luminosity AGN in massive nearby galaxies do not always manifest themselves as detectable nuclei in the broad-band *HST* data (Lauer et al. 2005; Dullo & Graham 2012; Dullo 2019). There are a total of 11 optically active core-Sérsic galaxies in LeMMINGs sample (Dullo et al. 2023a). Out of these, 9/11 are radio detected (Baldi et al. 2018, 2021a) and 10/11 are X-ray detected (Williams et al. 2022). However, only 2 (18 per cent) of these active core-Sérsic galaxies (NGC 3193 and NGC 4278) exhibit nuclei in our analysis of the galaxies' broad-band *HST* imaging data (see Table A2). Furthermore, the sizes of NGC 3193 and NGC 4278 nuclei, with $R_{e,nuc} \sim 63$ and 5 pc, respectively, do not guarantee that they are compact point sources (AGN) with sizes smaller than any plausible NSCs. We therefore argue that all the optical/near-IR flux for our core-Sérsic nuclei, seen in the broad-band *HST* images, cannot be explained solely by the low-luminosity AGN. In some cases, AGN alone can account for the nuclei observed in certain core-Sérsic galaxies, such as M87 (e.g. Ravindranath et al. 2001; Ferrarese et al. 2006b; Prieto et al. 2016; Dullo 2019).

3.2.3 *Hybrid nuclei demography*

Fig. 6 shows the incidence of hybrid (NSC+AGN) nuclei, optical and radio AGN, and all nuclei as a function of bulge stellar mass ($M_{*,bulge}$) and galaxy stellar mass ($M_{*,gal}$). We define the hybrid nuclei fraction as the ratio between the number of galaxies hosting a hybrid nucleus and the total number of galaxies under consideration (i.e. 149 galaxies; see Section 3.1). While nuclei are defined as distinct central light excesses with respect to the inward extrapolation of outer Sérsic or core-Sérsic profiles (Section 2.2), we note that the identification of radio and optical AGN relies on the nuclear radio continuum emission and optical emission-line data (Section 2.1).

The fraction of galaxies hosting hybrid nuclei increases with increasing $M_{*,bulge}$ and $M_{*,gal}$, peaking at intermediate masses ($M_{*,bulge}/M_{*,gal} \sim 10^{10.0} - 10^{11.4}$ M$_\odot$/$10^{10.6} - 10^{11.8}$ M$_\odot$) before declining at higher stellar masses. We find that low mass galaxies with $M_{*,gal} \lesssim 10^{10.6}$ M$_\odot$ show comparable frequencies of hybrid nuclei and optical AGN. However, above this mass (i.e. $M_{*,gal} \gtrsim 10^{10.6}$ M$_\odot$) galaxies are more likely to show evidence of AGN activity rather than hosting hybrid nuclei.

As noted in the introduction, Seth et al. (2008) used radio, X-ray, and optical spectroscopic observations and from the optical spectra, they reported that 10 per cent of their sample galaxies with NSCs host both AGN and nuclear star clusters. Using *Chandra* X-ray observations for a sample of 98 (47 late-types and 51 early-types) galaxies with NSCs, Foord et al. (2017) reported that ∼11.2 per cent harbour hybrid nuclei (see also Gallo et al. 2010). All the nuclei in our sample of nucleated galaxies with an optical AGN are classified as hybrid nuclei. However, we determine the lower limit for the fraction of hybrid nuclei in the nucleated sample by adopting a criterion that requires the use of a multiband signature, which combines radio, X-ray, and optical spectra data. Our criterion is more stringent than those used by Seth et al. (2008) and Foord et al. (2017). We identify 30 nucleated LeMMINGs hosts that are optically active, radio detected, and X-ray luminous ($L_X > 10^{39}$ erg s^{-1}). Relying solely on optical and X-ray AGN diagnostics, we find that 39 nucleated LeMMINGs galaxies are optically active and X-ray luminous ($L_X > 10^{39}$ erg s^{-1}). We do not suggest that the sources with $L_X < 10^{39}$ erg s^{-1} are inactive. Instead, a high X-ray core luminosity ($L_X > 10^{39}$ erg s^{-1}) likely indicate the presence of a low-luminosity AGN (Williams et al. 2022).

To summarize, our observations suggest that at least 30 per cent of the nucleated LeMMINGs galaxies harbour a hybrid nucleus containing both an NSC and AGN and they exhibit a wide range in morphology (ellipticals to late-type spirals, Sc) and in stellar mass, $M_{*,bulge}(M_{*,gal}) \sim 10^8 - 10^{11.8}(10^9 - 10^{12}$ M$_\odot$). While the hosts of 29 of the 30 hybrid nuclei mentioned above are within 78 Mpc, the host galaxy of the remaining hybrid nucleus is at 107 Mpc. Excluding this furthest galaxy, we measure a number density of $(1.5 \pm 0.4) \times 10^{-5}$ Mpc^{-3} for the sample of 29 galaxies.

The hybrid nucleus fraction we measured is at least a factor of three higher than that previously reported (e.g. Seth et al. 2008; Foord et al. 2017). As mentioned in the introduction, these previous works relied on a literature compilation of nuclei identified in *HST* imaging data. In contrast, we performed detailed 1D and 2D decompositions of the host galaxy *HST* data to identify the nuclei. Also, our AGN diagnostics capitalize on homogeneously derived, high-quality *e*-MERLIN radio, *Chandra* X-ray, and optical emission line data. Furthermore, with regards to the co-existence of NSCs and SMBHs, both active and inactive, our sample of 100 nucleated galaxies includes 40 galaxies with measured SMBH masses. These 40 SMBH masses are determined using gas dynamics, stellar dynamics, megamasers, or reverberation mapping (Dullo et al. 2023b).

3.2.4 *Do NSCs enhance AGN activity?*

Having established the AGN fraction in NSCs (i.e. in our nucleated galaxies), we examine here whether it is different in non-nucleated galaxies. Naiman et al. (2015) reported that the presence of NSCs

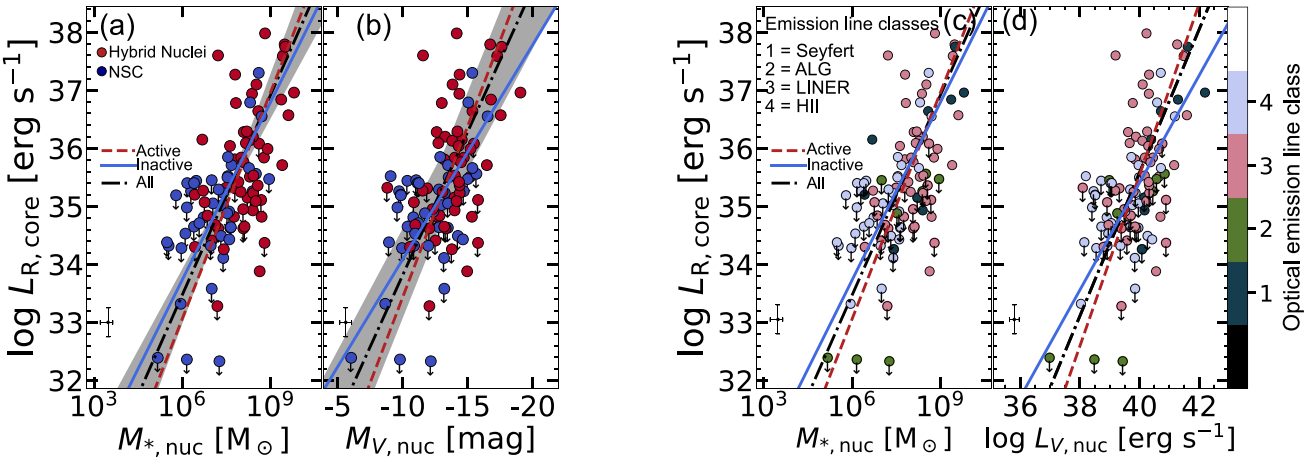

Figure 7. Radio scaling relations for our sample of 100 nucleated galaxies. Left panels: the 1.5 GHz radio core luminosity from *e*-MERLIN ($L_{R,core}$), Table A2, is plotted as a function of (a) the nucleus' stellar mass ($M_{*,nuc}$) and (b) V-band absolute magnitude ($M_{V,nuc}$), colour-coded by nucleus types. Right panels: the radio scaling relations by separating the galaxies based on their spectral classes. To allow better comparison with earlier studies on AGN, we converted the nuclei absolute magnitudes into V-band nuclei luminosities ($L_{V,nuc}$) in units of solar luminosity ($L_{V,\odot}$) such that $L_{V,nuc} = (L_{V,\odot})10^{(0.4)(M_{V,\odot}-M_{V,nuc})}$, where $M_{V,\odot} = 4.81$ (Willmer 2018) and $L_{V,\odot} = 4.4 \times 10^{32}$ erg s^{-1} (O'Shaughnessy et al. 2012). The nuclei that are not radio-detected with *e*-MERLIN at 1.5 GHz, and thus have 3σ upper limit $L_{R,core}$ values, are shown by downward arrows. The dashed, solid, and dash-dotted lines are BCES bisector regressions for the active galaxies (i.e. hybrid nuclei, red circles), inactive galaxies (i.e. NSCs, blue circles), and all nuclei, respectively. A typical error bar associated with the data points is shown at the bottom of each panel.

can facilitate the fuelling of the embedded SMBHs, by funnelling gas towards the innermost regions, during galaxy mergers. However, González Delgado et al. (2008) did not find a trend between nucleation and optical emission-line types. Foord et al. (2017) also argued that NSCs do not enhance accretion-powered emission from the central SMBH. Here, we use the optical, X-ray, and radio data from LeMMINGs and re-investigate the issue. When not controlling for bulge/galaxy mass and comparing our nucleated and the full *HST* sample (Dullo et al. 2023b), we find a slight increase in the Seyfert and LINER fractions and a slight decrease in ALG and H II fractions for our sample containing only nucleated galaxies. The optical emission-line class breakdown for the 100 nucleated galaxies is Seyferts (9 ± 3 per cent), ALGs (9 ± 3 per cent), LINERs (48 ± 7 per cent), and H II galaxies (34 ± 6 per cent). In comparison, the full LeMMINGs galaxies[2] with *HST* data (see Sections 2.4 and 3.1) consists of Seyferts (6 ± 2 per cent), ALGs (12 ± 3 per cent), LINERs (42 ± 5 per cent), and H II galaxies (40 ± 5 per cent).

Our nucleated sample also has a slightly higher radiodetection rate than the full *HST* sample, but the two samples are indistinguishable in terms of X-ray-detection rate. The radiodetection fraction for the 100 nucleated LeMMINGs galaxies is 50 ± 7 per cent, compared to 45± 5 per cent for LeMMINGs galaxies with *HST* data. We find X-ray detection fractions of 81 ± 10 and 78 ± 7 for the 84 nucleated LeMMINGs galaxies with X-ray data available and the LeMMINGs *HST* sample, respectively. Intriguingly, while ALG and LINER hosts constitute 87 per cent of the massive ($M_{*,bulge} \gtrsim 10^{11}$ M$_\odot$) objects in our sample of 149 galaxies, none (0/7) of the massive ALGs contains an NSC, whereas 14/24 (58 per cent) of massive LINERs are nucleated.

In general, our findings lend further support to the suggestion by Naiman et al. (2015) that NSCs may enhance accretion on to the central SMBH, by channelling gas towards the innermost regions (see also Chang et al. 2007). However, the trends of AGN activity and radio detection for the nucleated and full *HST* samples are associated with large uncertainties assuming Poissonian errors.

[2]For comparison the parent LeMMINGs sample of 280 galaxies contains 6.4 per cent Seyferts, 10.0 per cent ALGs, 33.6 per cent LINERs, and 50.0 per cent H II.

4 RADIO AND X-RAY SCALING RELATIONS FOR NUCLEI

In Dullo et al. (2023a), we showed that active and inactive nuclei hosts follow considerably different radio core luminosity ($L_{R,core}$)–$M_{*,bulge}$, $L_{R,core} - M_{V,bulge}$, and $L_{R,core}$–σ correlations, with turnovers at $M_{*,bulge} \sim 10^{9.8\pm0.3}$ M$_\odot$, $M_{V,bulge} \sim -18.5 \pm 0.3$ mag, and $\sigma \sim 85 \pm 5$ km s^{-1}. The turnovers signify a shift from AGN-dominated nuclear radio emission in more massive bulges to stellar-driven emission in low-mass bulges. Similarly, Saikia, Körding & Falcke (2015) and Baldi et al. (2021b) reported broken relations between $L_{R,core}$ and the optical [O III] λ5007 Å luminosity ($L_{[O\,iii]}$) and M_{BH} for local galaxies. They found that below a threshold mass of $M_{BH} \sim 10^{6.5}$ M$_\odot$ the nuclear radio emission is predominantly associated with stellar processes, whereas AGN-driven sources are found to be dominant at higher masses. On the other hand, Williams et al. (2022) found that optically active and inactive LeMMINGs galaxies together form single $L_X - M_{BH}$ and $L_X - L_{[O\,iii]}$ relations across the entire galaxy mass and luminosity ranges. Building on these earlier works, we investigate whether the mass or luminosity of the nucleus, derived from broad-band optical and near-IR *HST* images, correlates with the radio and X-ray core luminosities. We also examine how these relations vary depending on the nuclear activity of their hosts.

4.1 $L_{R,core} - M_{*,nuc}$ and $L_{R,core} - M_{V,nuc}$

Fig. 7 shows relations between $L_{R,core}$ and nucleus mass ($M_{*,nuc}$) and absolute V-band nucleus magnitude ($M_{V,nuc}$) for our sample of 100 nucleated LeMMINGs galaxies. The data points are colour-coded based on the three classes of nucleus introduced in Section 3.2

Table 5. Scaling relations between radio and X-ray core luminosities and the mass and luminosity of nuclei.

Relation	BCES bisector fit	r_s/P-value	r_p/P-value	δ_{horiz} (dex)	Sample
Hybrid nuclei (NSC + AGN; active galaxies)					
$L_{R,core} - M_{*,nuc}$	$\log\left(\frac{L_{R,core}}{erg\ s^{-1}}\right) = (1.30 \pm 0.23)\log\left(\frac{M_{*,nuc}}{6.3\times10^7 M_\odot}\right) + (35.40 \pm 0.17)$	$0.46/3.86 \times 10^{-4}$	$0.49/1.42 \times 10^{-4}$	0.92	57
$L_{R,core} - M_{V,nuc}$	$\log\left(\frac{L_{R,core}}{erg\ s^{-1}}\right) = (-0.59 \pm 0.12)\left(M_{V,nuc} + 13.9\right) + (35.73 \pm 0.17)$	$-0.46/4.11 \times 10^{-4}$	$-0.50/7.75 \times 10^{-5}$	–	57
$L_X - M_{*,nuc}$	$\log\left(\frac{L_X}{erg\ s^{-1}}\right) = (1.44 \pm 0.18)\log\left(\frac{M_{*,nuc}}{1.6\times10^8 M_\odot}\right) + (39.98 \pm 0.16)$	$0.52/1.25 \times 10^{-4}$	$0.59/6.70 \times 10^{-6}$	0.80	50
$L_X - M_{V,nuc}$	$\log\left(\frac{L_X}{erg\ s^{-1}}\right) = (-0.68 \pm 0.09)\left(M_{V,nuc} + 14.0\right) + (39.90 \pm 0.22)$	$-0.40/3.66 \times 10^{-3}$	$-0.51/1.40 \times 10^{-4}$	–	50
NSCs (inactive galaxies)					
$L_{R,core} - M_{*,nuc}$	$\log\left(\frac{L_{R,core}}{erg\ s^{-1}}\right) = (1.02 \pm 0.16)\log\left(\frac{M_{*,nuc}}{1.6\times10^7 M_\odot}\right) + (34.96 \pm 0.22)$	$0.60/2.09 \times 10^{-5}$	$0.56/9.63 \times 10^{-5}$	0.94	43
$L_{R,core} - M_{V,nuc}$	$\log\left(\frac{L_{R,core}}{erg\ s^{-1}}\right) = (-0.37 \pm 0.09)\left(M_{V,nuc} + 13.1\right) + (35.23 \pm 0.16)$	$-0.55/1.26 \times 10^{-4}$	$-0.58/4.53 \times 10^{-5}$	–	43
$L_X - M_{*,nuc}$	$\log\left(\frac{L_X}{erg\ s^{-1}}\right) = (1.28 \pm 0.24)\log\left(\frac{M_{*,nuc}}{1.6\times10^7 M_\odot}\right) + (38.61 \pm 0.19)$	$0.53/1.36 \times 10^{-3}$	$0.48/3.80 \times 10^{-3}$	0.84	34
$L_X - M_{V,nuc}$	$\log\left(\frac{L_X}{erg\ s^{-1}}\right) = (-0.63 \pm 0.12)\left(M_{V,nuc} + 12.0\right) + (38.37 \pm 0.22)$	$-0.60/2.06 \times 10^{-4}$	$-0.47/4.35 \times 10^{-3}$	–	34

Note. 1.5 GHz radio core luminosity from *e*-MERLIN ($L_{R,core}$) and (0.3–10 keV) *Chandra* X-ray core luminosity (L_X) as a function of nucleus stellar mass ($M_{*,nuc}$) and nucleus absolute magnitude ($M_{V,nuc}$). We present our BCES bisector regression fits to the galaxy data, the Spearman and Pearson correlation coefficients (r_s and r_p, respectively) and the corresponding serendipitous correlation probabilities. The horizontal rms scatter in the log $M_{*,nuc}$ direction is denoted with δ_{horiz}.

[Figs 7(a) and (b)]. We also divided the sample based on optical emission-line classifications (Baldi et al. 2018, 2021a) and transformed the nuclei absolute magnitudes into V-band nuclei luminosities ($L_{V,nuc}$) in units of solar luminosity ($L_{V,\odot}$) for better comparison with earlier studies on AGN (e.g. Baldi et al. 2010), Figs 7(c) and 7(d). In doing so, we use the equation $L_{V,nuc} = (L_{V,\odot})10^{(0.4)(M_{V,\odot} - M_{V,nuc})}$, where $M_{V,\odot} = 4.81$ (Willmer 2018) and $L_{V,\odot} = 4.4 \times 10^{32}$ erg s^{-1} (O'Shaughnessy, Kopparapu & Belczynski 2012).

We fit the BCES bisector regressions to the ($L_{R,core}$, $M_{*,nuc}$) and ($L_{R,core}$, $M_{V,nuc}$) data sets. The BCES method allows for errors in the fitted variables to be taken into account. The implementation of the BCES routine (Akritas & Bershady 1996) here is adapted from the PYTHON module by Nemmen et al. (2012). While the results from the BCES bisector regressions are presented throughout this paper, we find good agreement between the BCES bisector and orthogonal regression fits. The slopes and intercepts from the two methods are consistent within the 1σ uncertainties. We present the key radio scaling relations in Table 5.

Furthermore, half of our sample have $L_{R,core}$ upper limits, where the sources do not have a detectable nuclear radio emission with *e*-MERLIN at 1.5 GHz. We therefore performed a statistical censored analysis with the ASURV software package (Feigelson & Nelson 1985; Isobe, Feigelson & Nelson 1986), which accounts for upper limits (see Appendix A4). We find that the slopes and intercepts of the $L_{R,core} - M_{*,nuc}$ and $L_{R,core} - M_{V,nuc}$ relations from the censored and uncensored analyses agree within the quoted errors (Table 5 and Appendix A4). However, we note that the intercepts of the censored relations from the ASURV fits have large errors.

We find that $L_{R,core}$ correlates well with $M_{*,nuc}$ and $M_{V,nuc}$ (see also Balmaverde & Capetti 2006; Balmaverde, Capetti & Grandi 2006; Baldi et al. 2010). We measure the Spearman and Pearson correlation coefficients (r_s and r_p) to quantify the strength of the correlations. For the $L_{R,core} - M_{*,nuc}$ relations, we find $r_s/r_p \sim 0.59/0.60$ and a very low probability P of the null hypothesis ($\sim 10^{-11} - 10^{-10}$), see Table 5. Similarly, the $L_{R,core} - M_{V,nuc}$ relations are such that $-r_s/-r_p \sim 0.55/0.59$ and $P \sim 10^{-10} - 10^{-9}$. We also derived the horizontal rms scatters in the log $M_{*,nuc}$ direction, finding $\delta_{horiz} \sim 0.92 - 0.96$ dex. NSCs and hybrid nuclei follow $L_{R,core} - L_{V,nuc}$ and $L_{R,core} - M_{*,nuc}$ relations with comparable level of scatter and strength.

Separating the sample into NSCs and hybrid nuclei (i.e. dividing the full sample into active and inactive) and running the BCES regressions yields relations where the slopes and intercepts for the two nuclei types are consistent with each other within the 1σ errors. These relations also agree, within the errors, with those for the full sample (Table 5 and Appendix A4). For the full sample, the BCES bisector regression fits yield near-linear $L_{R,core} - M_{*,nuc}$ and $L_{R,core} - L_{V,nuc}$ relations, see Appendix A4.

However, for nucleated galaxies of the same radio core luminosities, NSC tend to be less massive/luminous than hybrid nuclei (Fig. 7). There is also a tendency in the $L_{R,core} - M_{*,nuc}$, $L_{R,core} - M_{V,nuc}$ relations where the slopes for the hybrid nuclei are slightly steeper than those for the NSCs. This is reminiscent of the corresponding trend observed in the other $L_{R,core}$ scaling relations (i.e. $L_{R,core} - M_{*,bulge}$, $L_{R,core} - M_{V,bulge}$, $L_{R,core}$–σ, $L_{R,core} - M_{BH}$, and $L_{R,core} - L_{[O\,iii]}$) presented in Saikia et al. (2018), Baldi et al. (2021b), and Dullo et al. (2023a). While our regression analysis shows that NSCs and hybrid nuclei follow common relations within the errors in the $L_{R,core} - M_{*,nuc}$, $L_{R,core} - M_{V,nuc}$ diagrams, we believe this apparent unity of NSCs and hybrid nuclei is artificial and driven by the relatively low incidence of nucleation in low-mass, late-type galaxies, and massive early-type galaxies (Figs 4–8 and Section 3.1). These galaxies consequently have low representation in Fig. 7, which is also evident in Fig. 8, which displays the location of the 100 nucleated LeMMINGs galaxies and the remaining 73 LeMMINGs/*HST* galaxies which did not meet our criteria for having a nucleus (Section 2.4). If large numbers of low-mass, late-type galaxies are included in the sample, we suspect that hybrid nuclei, similar to active bulges, define $L_{R,core}$ scaling relations with slopes that are steeper than those for the NSCs (inactive galaxies). Note that Fig. 8 is a modified version of the $L_{R,core} - M_{*,bulge}$, $L_{R,core} - M_{V,bulge}$ diagrams from Dullo et al. (2023a, their fig. 8). The dashed and solid lines (Fig. 8) are the ordinary least-squares (OLS) bisector regressions for the optically active (AGN) galaxies (LINER and Seyfert) and optically inactive galaxies (H II and ALG), respectively.

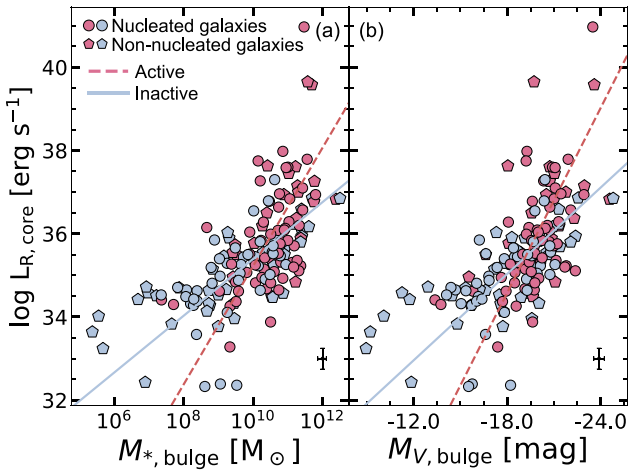

Figure 8. 1.5 GHz radio core luminosity from *e*-MERLIN ($L_{\rm R,core}$) is plotted against (a) bulge stellar mass ($M_{*,\rm bulge}$) and (b) absolute *V*-band bulge magnitude ($M_{V,\rm bulge}$) for our full sample of 173 galaxies with *HST* data. The plot is similar to that in Dullo et al. (2023a, their fig. 8), but here we separated the sample into nucleated galaxies (circles) and non-nucleated galaxies (pentagons) to highlight the importance non-nucleated galaxies, which are missing in Fig. 7, in defining the broken $L_{\rm R,core}$–$M_{*,\rm bulge}$, $L_{\rm R,core} - M_{V,\rm bulge}$ relations. The dashed line is our OLS bisector regression fit to the active (optical AGN) galaxies (LINERs and Seyferts), while the solid line is the OLS bisector fit to inactive galaxies (H II s and absorption line galaxies, ALGs). A typical error bar associated with the data points is shown at the bottom of each panel.

4.2 $L_{\rm X} - M_{*,\rm nuc}$ and $L_{\rm X} - M_{V,\rm nuc}$

In Fig. 9, we plot the (0.3−10 keV) X-ray core luminosity ($L_{\rm X}$) against $M_{*,\rm nuc}$ and $M_{V,\rm nuc}$ for our sample of the 84 nucleated galaxies with available *Chandra* X-ray data (Williams et al. 2022). Akin to Fig. 7, we show two plots where the galaxies are separated based on nucleus types and optical emission-line classifications (Fig. 9). Using our ($L_{\rm X}$, $M_{*,\rm nuc}$) and ($L_{\rm X}$, $M_{V,\rm nuc}$) data set, we perform BCES regressions to derive the $L_{\rm X} - M_{*,\rm nuc}$ and $L_{\rm X} - L_{V,\rm nuc}$ relations for NSCs and hybrid nuclei separately (Table 5). We also fit BCES bisector regressions to derive $L_{\rm X} - M_{*,\rm nuc}$ and $L_{\rm X} - M_{V,\rm nuc}$ relations for the full sample of 84 nucleated galaxies with X-ray data (see Appendix A4). We find that the values of the slopes and intercepts for the NSCs and hybrid nuclei and combined sample are consistent with each other within the 1σ errors. Out of the 84 nucleated sources, 16 have $L_{\rm X}$ upper limits. Overall, the slopes and intercepts for our $L_{\rm X}$ scaling relations from the censored ASURV regressions and non-censored BCES regressions are in fair agreement (Table 5).

The Spearman and Pearson correlation coefficients and the corresponding *P* values for the $L_{\rm X} - M_{*,\rm nuc}$ relations are $r_{\rm s} \sim 0.52 - 0.63$, $r_{\rm p} \sim 0.50 - 0.65$, and $P \sim 10^{-11} - 10^{-4}$. The $L_{\rm X} - M_{V,\rm nuc}$ relations are such that $-r_{\rm s} \sim 0.50 - 0.59$, $-r_{\rm p} \sim 0.51 - 0.58$, and $P \sim 10^{-9} - 10^{-7}$. For the $L_{\rm X} - M_{*,\rm nuc}$ and $L_{\rm X} - M_{V,\rm nuc}$ relations, the horizontal rms scatters in the log $M_{*,\rm nuc}$ direction are $\delta_{\rm horiz} \sim 0.80 - 0.86$ dex.

Our analysis shows that NSCs and hybrid nuclei unite to define single unbroken $L_{\rm X} - M_{*,\rm nuc}$ and $L_{\rm X} - M_{V,\rm nuc}$ correlations with overlapping uncertainties. This is in agreement with Williams et al. (2022) who found that optically active and inactive LeMMINGs galaxies together form single $L_{\rm X} - {\rm M_{BH}}$ and $L_{\rm X} - L_{[{\rm O}\,iii]}$ relations across the entire galaxy mass and luminosity ranges.

Finally, we investigate whether nuclei are more strongly correlated with $L_{\rm X}$ or $L_{\rm R,core}$, and find that $M_{*,\rm nuc}$ and $M_{V,\rm nuc}$ are similarly correlated with both $L_{\rm X}$ and $L_{\rm R,core}$. However, nuclei are more closely associated with $L_{\rm X}$ than $L_{\rm R,core}$, with respect to the rms scatters in the log $M_{*,\rm nuc}$ direction ($\delta_{\rm horiz}$), as the $L_{\rm X}$ relations have $\delta_{\rm horiz} \sim 0.80 - 0.83$ dex, which is smaller than those for the $L_{\rm R,core}$ relations ($\delta_{\rm horiz} \sim 0.92 - 0.96$ dex), see Table 5 and Appendix A4.

5 SUMMARY AND CONCLUSIONS

The *e*-MERLIN legacy survey (LeMMINGs, Beswick et al. 2014) is the deepest, high-resolution radio continuum survey of a statistically complete, sample of 280 nearby galaxies with *e*-MERLIN at 1.25−1.75 and 5 GHz. We have presented a study of the co-existence of nuclear star clusters (NSCs) and AGN in 100 nearby, nucleated LeMMINGs galaxies, including 10 elliptical, 25 lenticular, 63 spiral, and 2 irregular galaxies. In Dullo et al. (2023b), we studied photometric and structural properties of nearby galaxies by selecting all LeMMINGs galaxies with reliable *HST* imaging data, yielding a subsample of 173 galaxies, which were shown to be representative of the parent LeMMINGs sample. To identify the nuclei, we used high-resolution optical and near-infrared *HST* images and performed accurate 1D and 2D multicomponent decompositions of the stellar light distributions of the 173 LeMMINGs galaxies (into bulges, discs, depleted core, AGN, nuclear star clusters, bars, spiral arms, rings, and stellar haloes) using Sérsic and core-Sérsic models. From this analysis, we identified 100 nucleated galaxies that fulfilled our criteria for hosting a dense star cluster, a 'pure' AGN or a combination of both (Section 2.4). We have derived luminosities, stellar masses, and half-light radii for the nuclei.

Our detailed multicomponent decompositions of 65 LT+35 ET galaxies are improvements over the past literature, particularly, since past studies often fitted a two-component, nucleus+bulge model to the light distributions nucleated galaxies. Furthermore, there are only a few published photometric and structural studies on the nuclei of late-type galaxies with *HST* (Böker et al. 2002; Carollo et al. 2002; Georgiev & Böker 2014; Dullo et al. 2023b), see Table 4. Other improvements include our AGN diagnostics, where we combine the *HST* decomposition data with homogeneously derived, nuclear 1.5 GHz *e*-MERLIN radio, *Chandra* X-ray (0.3–10 keV) and optical emission-line data from LeMMINGs (Baldi et al. 2018, 2021a, b; Williams et al. 2022). The multiwavelength data used in this work span wide ranges in galaxy stellar mass and nuclear radio and X-ray luminosities: $M_{*,\rm gal} \sim 10^{8.7} - 10^{12}$ M$_\odot$, $L_{\rm R,core} \sim 10^{32} - 10^{40}$ erg s^{-1}, and $L_{\rm X} \sim 10^{35} - 10^{43}$ erg s^{-1}. To our knowledge, this work represents the most comprehensive multiwavelength investigation to date of the connection between NSCs and AGN in nearby galaxies.

Our principal conclusions are:

(i) We define the nucleation fraction ($f_{\rm nuc}$) as the relative incidence of nuclei in the sample under consideration. Among the sample of LeMMINGs galaxies with *HST* data and excluding the 24 questionable galaxies (see Section 2.4), we find $f_{\rm nuc}$ =100/149 (= 67 ± 7 per cent), in agreement with previous reports. When we treat the 24 excluded galaxies as non-nucleated then $f_{\rm nuc}$ =100/173 (= 58 ± 6 per cent) for the full LeMMINGs *HST* sample. We also find that $f_{\rm nuc}$ increases with increasing $M_{*,\rm bulge}$ and $M_{*,\rm gal}$, peaking at bulge masses $M_{*,\rm bulge} \sim 10^{9.4} - 10^{10.8}$ M$_\odot$ ($f_{\rm nuc}$ = 49/56 = 88 ± 13 per cent), before decreasing at higher stellar masses. Core-Sérsic galaxies exhibit a low incidence of nucleation, $f_{\rm nuc}$ = (10–20) ± 6 per cent. This figure supports the widely accepted hypothesis of core-Sérsic galaxy formation, where coalescing binary SMBHs not only scour

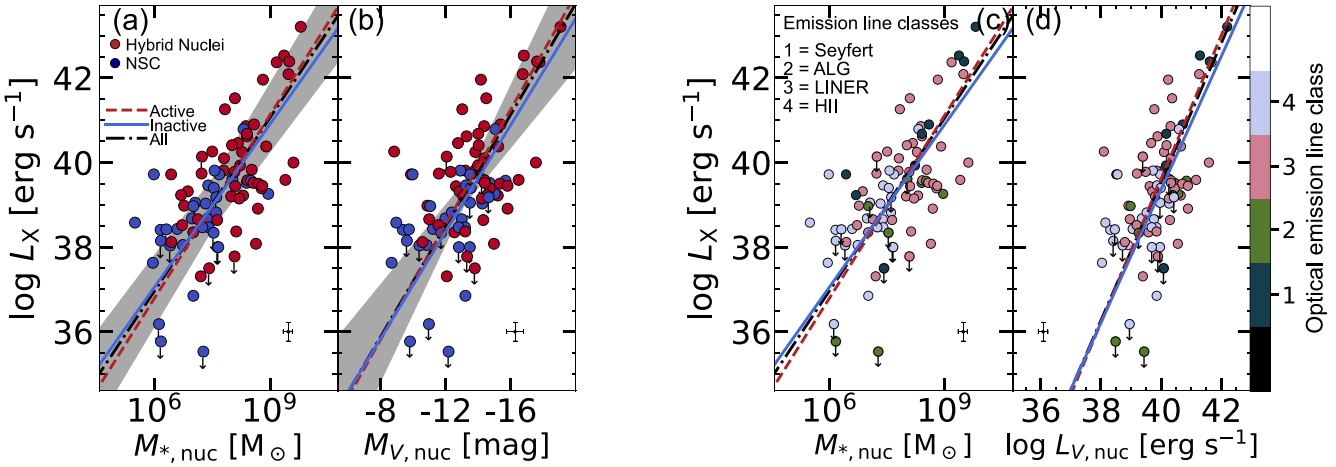

Figure 9. Similar to Fig. 7, but shown here are the correlations between the (0.3−10 keV) X-ray core luminosity ($L_{\rm X}$) and $M_{*,\rm nuc}$ and $M_{V,\rm nuc}/L_{V,\rm nuc}$ for the 84 nucleated galaxies in our sample with available *Chandra* X-ray data. Representative error bars are shown at the bottom of the panels.

the cores but also tidally disrupt any NSCs. In contrast, Sérsic galaxies show a much higher nucleation frequency ($f_{\rm nuc} = 98/129 = 76 \pm 8$ per cent).

(ii) We classify 43 nuclei in the sample as 'pure' NSCs, which are optically inactive. We argue that the bulk of the central light excesses in the optical or near-IR brightness profiles of these nuclei are of stellar origin. In contrast, 57 nuclei are optically active and classified as 'hybrid' (NSC+AGN). We suggest that the optical or near-IR flux of such nuclei likely results from contributions of both stellar and non-stellar emissions.

(iii) In order to determine the lower limit for the hybrid nucleus fraction in our sample, we employ AGN diagnostics that utilize a multiband signature. This method combines homogeneously derived, high fidelity *e*-MERLIN radio, *Chandra* X-ray, and optical emission-line data. We identify 30 nucleated galaxies in our nucleated sample that are optically active, radio detected, and X-ray luminous ($L_{\rm X} > 10^{39}$ erg s^{-1}). We conclude that our sample has a lower limit frequency for hybrid nuclei of $\sim$ 30 per cent. This figure is at least a factor of three higher than that previously reported (e.g. Seth et al. 2008; Foord et al. 2017). These previous works are based on a literature compilation of nuclei identified in *HST* imaging data. In contrast, our nuclei are identified uniformly using detailed 1D and 2D decompositions of the host galaxy *HST* data and multiwavelength data sets from LeMMINGs. We measure a lower limit number density of $(1.5 \pm 0.4) \times 10^{-5}$ Mpc^{-3} for hybrid nuclei. The fraction of galaxies hosting hybrid nuclei increases with $M_{*,\rm bulge}$ and $M_{*,\rm gal}$, peaking at intermediate masses ($M_{*,\rm bulge}/M_{*,\rm gal} \sim 10^{10.0} - 10^{11.4}$ M$_\odot$/$10^{10.6} - 10^{11.8}$ M$_\odot$), before declining at higher stellar masses. For our *HST* sample of 149 galaxies, comprising both nucleated and non-nucleated types, we find that low mass galaxies with $M_{*,\rm gal} \lesssim 10^{10.6}$ M$_\odot$ exhibit a similar occurrence of hybrid nuclei and optical AGN activity. However, above this mass (i.e. $M_{*,\rm gal} \gtrsim 10^{10.6}$ M$_\odot$) galaxies are more likely to exhibit evidence of optical and radio AGN activities rather than hosting hybrid nuclei.

(iv) Comparing our nucleated and the full LeMMINGs *HST* sample and not controlling for bulge/galaxy mass, we find a slight increase in the Seyfert and LINER fractions and a slight decrease in ALG and H II fractions for our sample containing only nucleated galaxies. Our nucleated sample also has a slightly higher radiodetection rate than our full *HST* sample, but the two samples are statistically indistinguishable in terms of X-ray detection rate. Our findings suggest that NSCs may enhance accretion on to the central SMBH, by funnelling gas towards the innermost regions (e.g. Naiman et al. 2015). Nevertheless, we caution that further investigation using a larger sample of galaxies is needed to draw firm conclusions, given the large Poisson errors associated with these trends.

(v) Scaling relations involving carefully acquired masses/luminosities of nuclei, observed in the broad-band optical and near-IR *HST* images, and the radio and X-ray core luminosities are provided in Section 4. Our investigation of radio core luminosities suggests that NSCs and hybrid nuclei follow common relations in the $L_{\rm R,core} - M_{*,\rm nuc}$, $L_{\rm R,core} - M_{V,\rm nuc}$ diagrams. However, we suspect that the apparent unity among all types of nuclei in $L_{\rm R,core}$ scaling diagrams might be driven by the relatively low incidence of nucleation in low-mass late-type galaxies and massive early-type galaxies (Figs 4–8 and Section 3.1). Once large numbers of low-mass late-type galaxies are included, we argue that hybrid nuclei, akin to active bulges, define $L_{\rm R,core}$ scaling relations with slopes steeper than those for the 'pure' NSCs (inactive galaxies). Furthermore, our analysis reveals that NSCs and hybrid nuclei collectively follow single unbroken (log-linear) $L_{\rm X} - M_{*,\rm nuc}$ and $L_{\rm X} - M_{V,\rm nuc}$ relations.

ACKNOWLEDGEMENTS

We thank the referee for a timely and supportive report that improved this manuscript. AGdP acknowledges financial support under grant No. PID2022-138621NB-I00. AA acknowledges financial support from the Spanish Ministerio de Ciencia e Innovación (grant PID2020-117404GB-C21) and from the grant CEX2021-001131-S funded by MCIN/AEI/ 10.13039/50110001103. JHK's research is co-funded by the European Union. Views and opinions expressed are however those of the author(s) only and do not necessarily reflect those of the European Union. Neither the European Union nor the granting authority can be held responsible for them. JHK acknowledges support from the Agencia Estatal de Investigación del Ministerio de Ciencia, Innovación y Universidades (MCIU/AEI) under the grant 'The structure and evolution of galaxies and their outer regions' and the European Regional Development Fund (ERDF) with reference PID2022-136505NB-I00/10.13039/501100011033. Based on observations made with the NASA/ESA *Hubble Space Telescope*, and obtained from the Hubble Legacy Archive, which is a collaboration

between the Space Telescope Science Institute (STScI/NASA), the Space Telescope European Coordinating Facility (ST-ECF/ESA), and the Canadian Astronomy Data Centre (CADC/NRC/CSA). We would like to acknowledge the support from the *e*-MERLIN Legacy project 'LeMMINGs', upon which this study is based. *e*-MERLIN, and formerly, MERLIN, is a National Facility operated by the University of Manchester at Jodrell Bank Observatory on behalf of the STFC. We acknowledge Jodrell Bank Centre for Astrophysics, which is funded by the STFC. The scientific results reported in this article are based in part on observations made by the *Chandra* X-ray Observatory and published previously in cited articles. This research has made use of the NASA/IPAC Extragalactic Database (NED), which is operated by the Jet Propulsion Laboratory, California Institute of Technology, under contract with the National Aeronautics and Space Administration.

This work has made use of NUMPY (van der Walt, Colbert & Varoquaux 2011), MATPLOTLIB (Hunter 2007), and ASTROPY, a community-developed core PYTHON package for Astronomy (Astropy Collaboration 2013, 2018), ASTROQUERY (Ginsburg et al. 2019), CUBEHELIX (Green 2011), JUPYTER (Kluyver et al. 2016), SCIPY (Virtanen et al. 2020), and of TOPCAT (i.e. 'Tool for Operations on Catalogues And Tables', Taylor 2005).

DATA AVAILABILITY

The data underlying this article are available in the article.

REFERENCES

Akritas M. G., Bershady M. A., 1996, ApJ, 470, 706
Antonini F., Barausse E., Silk J., 2015, ApJ, 812, 72
Antonini F., Gieles M., Gualandris A., 2019, MNRAS, 486, 5008
Askar A., Davies M. B., Church R. P., 2021, MNRAS, 502, 2682
Astropy Collaboration 2013, A&A, 558, A33
Astropy Collaboration 2018, AJ, 156, 123
Balcells M., Graham A. W., Domínguez-Palmero L., Peletier R. F., 2003, ApJ, 582, L79
Balcells M., Graham A. W., Peletier R. F., 2007, ApJ, 665, 1084
Baldassare V. F., Reines A. E., Gallo E., Greene J. E., 2017, ApJ, 850, 196
Baldassare V. F., Stone N. C., Foord A., Gallo E., Ostriker J. P., 2022, ApJ, 929, 84
Baldi R. D. et al., 2010, ApJ, 725, 2426
Baldi R. D. et al., 2018, MNRAS, 476, 3478
Baldi R. D. et al., 2021a, MNRAS, 500, 4749
Baldi R. D. et al., 2021b, MNRAS, 508, 2019
Balmaverde B., Capetti A., 2006, A&A, 447, 97
Balmaverde B., Capetti A., Grandi P., 2006, A&A, 451, 35
Barth A. J., Ho L. C., Rutledge R. E., Sargent W. L. W., 2004, ApJ, 607, 90
Becker R. H., White R. L., Helfand D. J., 1995, ApJ, 450, 559
Bekki K., Graham A. W., 2010, ApJ, 714, L313
Beswick R., Argo M. K., Evans R., McHardy I., Williams D. R. A., Westcott J., 2014, in Proc. Sci., 12th European VLBI Network Symposium and Users Meeting (EVN 2014). Cagliari, Italy, p. 10
Birchall K. L., Watson M. G., Aird J., 2020, MNRAS, 492, 2268
Böker T., Laine S., van der Marel R. P., Sarzi M., Rix H.-W., Ho L. C., Shields J. C., 2002, AJ, 123, 1389
Böker T., Sarzi M., McLaughlin D. E., van der Marel R. P., Rix H.-W., Ho L. C., Shields J. C., 2004, AJ, 127, 105
Buttiglione S., Capetti A., Celotti A., Axon D. J., Chiaberge M., Macchetto F. D., Sparks W. B., 2010, A&A, 509, A6
Carollo C. M., Stiavelli M., de Zeeuw P. T., Mack J., 1997, AJ, 114, 2366
Carollo C. M., Stiavelli M., Mack J., 1998, AJ, 116, 68
Carollo C. M., Stiavelli M., Seigar M., de Zeeuw P. T., Dejonghe H., 2002, AJ, 123, 159
Chang P., Murray-Clay R., Chiang E., Quataert E., 2007, ApJ, 668, 236
Côté P. et al., 2006, ApJS, 165, 57
den Brok M. et al., 2014, MNRAS, 445, 2385
den Brok M. et al., 2015, ApJ, 809, 101
de Vaucouleurs G., 1959, Handb. Phys., 53, 275
de Vaucouleurs G., de Vaucouleurs A., Corwin H. G. J., 1976, Second reference catalogue of bright galaxies. Containing information on 4,364 galaxies with references to papers published between 1964 and 1975. Univ. Texas Press, Austin
de Vaucouleurs G., de Vaucouleurs A., Corwin H. G. J., Buta R. J., Paturel G., Fouqué P., 1991, Third Reference Catalogue of Bright Galaxies. Volume I: Explanations and references. Volume II: Data for galaxies between 0^h and 12^h. Volume III: Data for galaxies between 12^h and 24^h. Springer, New York
Driver S. P., Popescu C. C., Tuffs R. J., Graham A. W., Liske J., Baldry I., 2008, ApJ, 678, L101
Dullo B. T., 2019, ApJ, 886, 80
Dullo B. T., Graham A. W., 2012, ApJ, 755, 163
Dullo B. T., Graham A. W., 2013, ApJ, 768, 36
Dullo B. T., Graham A. W., 2014, MNRAS, 444, 2700
Dullo B. T., Martínez-Lombilla C., Knapen J. H., 2016, MNRAS, 462, 3800
Dullo B. T., Graham A. W., Knapen J. H., 2017, MNRAS, 471, 2321
Dullo B. T. et al., 2018, MNRAS, 475, 4670
Dullo B. T. et al., 2019, ApJ, 871, 9
Dullo B. T. et al., 2023a, MNRAS, 522, 3412
Dullo B. T. et al., 2023b, A&A, 675, A105
Erwin P., 2015, ApJ, 799, 226
Event Horizon Telescope Collaboration 2022, ApJ, 930, L12
Feigelson E. D., Nelson P. I., 1985, ApJ, 293, 192
Feldmeier A. et al., 2014, A&A, 570, A2
Ferrarese L., Ford H., 2005, Space Sci. Rev., 116, 523
Ferrarese L. et al., 2006a, ApJS, 164, 334
Ferrarese L. et al., 2006b, ApJ, 644, L21
Ferrarese L. et al., 2020, ApJ, 890, 128
Filippenko A. V., Ho L. C., 2003, ApJ, 588, L13
Filippenko A. V., Sargent W. L. W., 1985, ApJS, 57, 503
Filippenko A. V., Sargent W. L. W., 1989, ApJ, 342, L11
Foord A., Gallo E., Hodges-Kluck E., Miller B. P., Baldassare V. F., Gültekin K., Gnedin O. Y., 2017, ApJ, 841, 51
Freedman W. L. et al., 2019, ApJ, 882, 34
Gallo E., Treu T., Marshall P. J., Woo J.-H., Leipski C., Antonucci R., 2010, ApJ, 714, 25
Georgiev I. Y., Böker T., 2014, MNRAS, 441, 3570
Georgiev I. Y., Böker T., Leigh N., Lützgendorf N., Neumayer N., 2016, MNRAS, 457, 2122
Ghez A. M., Klein B. L., Morris M., Becklin E. E., 1998, ApJ, 509, 678
Gillessen S., Eisenhauer F., Trippe S., Alexander T., Genzel R., Martins F., Ott T., 2009, ApJ, 692, 1075
Ginsburg A. et al., 2019, AJ, 157, 98
Gnedin O. Y., Ostriker J. P., Tremaine S., 2014, ApJ, 785, 71
González Delgado R. M., Pérez E., Cid Fernandes R., Schmitt H., 2008, AJ, 135, 747
Graham A. W., 2016, in Laurikainen E., Peletier R., Gadotti D., eds, Astrophysics and Space Science Library Vol. 418, Galactic Bulges. Springer, Cham, p. 263
Graham A. W., Guzmán R., 2003, AJ, 125, 2936
Graham A. W., Spitler L. R., 2009, MNRAS, 397, 2148
Graham A. W., Erwin P., Trujillo I., Asensio Ramos A., 2003, AJ, 125, 2951
Grant N. I., Kuipers J. A., Phillipps S., 2005, MNRAS, 363, 1019
Green D. A., 2011, Bull. Astron. Soc. India, 39, 289
Greene J. E., Ho L. C., 2004, ApJ, 610, 722
Ho L. C., Filippenko A. V., Sargent W. L., 1995, ApJS, 98, 477
Ho L. C., Filippenko A. V., Sargent W. L. W., 1997a, ApJS, 112, 315
Ho L. C., Filippenko A. V., Sargent W. L. W., Peng C. Y., 1997b, ApJS, 112, 391
Ho L. C., Filippenko A. V., Sargent W. L. W., 1997c, ApJ, 487, 568
Hopkins P. F., Cox T. J., Dutta S. N., Hernquist L., Kormendy J., Lauer T. R., 2009, ApJS, 181, 135

Hoyer N., Neumayer N., Georgiev I. Y., Seth A. C., Greene J. E., 2021, MNRAS, 507, 3246
Hoyer N., Neumayer N., Seth A. C., Georgiev I. Y., Greene J. E., 2023, MNRAS, 520, 4664
Hubble E. P., 1926, ApJ, 64, 321
Hunter J. D., 2007, Comput. Sci. Eng., 9, 90
Ibata R. A. et al., 2013, Nature, 493, 62
Isobe T., Feigelson E. D., Nelson P. I., 1986, ApJ, 306, 490
Karachentsev I. D., Karachentseva V. E., Huchtmeier W. K., Makarov D. I., 2004, AJ, 127, 2031
Kewley L. J., Groves B., Kauffmann G., Heckman T., 2006, MNRAS, 372, 961
King I., 1962, AJ, 67, 471
King I. R., 1966, AJ, 71, 64
Kluyver T. et al., 2016, in Loizides F., Schmidt B., eds, Positioning and Power in Academic Publishing: Players, Agents and Agendas. IOS Press BV, Amsterdam, p. 87
Kormendy J., Ho L. C., 2013, ARA&A, 51, 511
Kroupa P., Subr L., Jerabkova T., Wang L., 2020, MNRAS, 498, 5652
Larsen S. S., 1999, A&AS, 139, 393
Lauer T. R. et al., 1995, AJ, 110, 2622
Lauer T. R. et al., 2005, AJ, 129, 2138
Leigh N., Böker T., Knigge C., 2012, MNRAS, 424, 2130
Lotz J. M., Miller B. W., Ferguson H. C., 2004, ApJ, 613, 262
Magorrian J. et al., 1998, AJ, 115, 2285
Mezcua M., Civano F., Marchesi S., Suh H., Fabbiano G., Volonteri M., 2018, MNRAS, 478, 2576
Naiman J. P., Ramirez-Ruiz E., Debuhr J., Ma C. P., 2015, ApJ, 803, 81
Nandi P., Stalin C. S., Saikia D. J., Muneer S., Mountrichas G., Wylezalek D., Sagar R., Kissler-Patig M., 2023, ApJ, 950, 81
Nemmen R. S., Georganopoulos M., Guiriec S., Meyer E. T., Gehrels N., Sambruna R. M., 2012, Science, 338, 1445
Neumayer N., Walcher C. J., 2012, Adv. Astron., 2012, 709038
Neumayer N., Seth A., Böker T., 2020, A&AR, 28, 4
Nguyen D. D. et al., 2018, ApJ, 858, 118
O'Shaughnessy R., Kopparapu R. K., Belczynski K., 2012, Class. Quantum Gravity, 29, 145011
Panessa F., Baldi R. D., Laor A., Padovani P., Behar E., McHardy I., 2019, Nat. Astron., 3, 387
Pechetti R., Seth A., Neumayer N., Georgiev I., Kacharov N., den Brok M., 2020, ApJ, 900, 32
Penny S. J. et al., 2018, MNRAS, 476, 979
Phillips A. C., Illingworth G. D., MacKenty J. W., Franx M., 1996, AJ, 111, 1566
Planck Collaboration VI 2020, A&A, 641, A6
Poulain M. et al., 2021, MNRAS, 506, 5494
Prieto M. A., Fernández-Ontiveros J. A., Markoff S., Espada D., González-Martín O., 2016, MNRAS, 457, 3801
Ravindranath S., Ho L. C., Peng C. Y., Filippenko A. V., Sargent W. L. W., 2001, AJ, 122, 653
Reines A. E., Sivakoff G. R., Johnson K. E., Brogan C. L., 2011, Nature, 470, 66
Richstone D. et al., 1998, Nature, 395, A14
Riess A. G., Casertano S., Yuan W., Macri L. M., Scolnic D., 2019, ApJ, 876, 85
Román J., Sánchez-Alarcón P. M., Knapen J. H., Peletier R., 2023, A&A, 671, L7
Saikia P., Körding E., Falcke H., 2015, MNRAS, 450, 2317
Saikia P., Körding E., Coppejans D. L., Falcke H., Williams D., Baldi R. D., Mchardy I., Beswick R., 2018, A&A, 616, A152
Sánchez-Janssen R. et al., 2019, ApJ, 878, 18
Sandage A., Tammann G. A., 1981, A Revised Shapley-Ames Catalog of Bright Galaxies. Carnegie Inst. of Washington, Washington
Sartori L. F., Schawinski K., Treister E., Trakhtenbrot B., Koss M., Shirazi M., Oh K., 2015, MNRAS, 454, 3722
Scarlata C. et al., 2004, AJ, 128, 1124
Schlafly E. F., Finkbeiner D. P., 2011, ApJ, 737, 103
Schödel R., Feldmeier A., Kunneriath D., Stolovy S., Neumayer N., Amaro-Seoane P., Nishiyama S., 2014, A&A, 566, A47
Sérsic J. L., 1963, Bol. Asoc. Argentina Astron. Plata Argentina, 6, 41
Sérsic J. L., 1968, Atlas de Galaxias Australes. Observatorio Astronómico, Córdoba, Argentina
Seth A. C., Dalcanton J. J., Hodge P. W., Debattista V. P., 2006, AJ, 132, 2539
Seth A., Agüeros M., Lee D., Basu-Zych A., 2008, ApJ, 678, 116
Seth A. C., Neumayer N., Böker T., 2020, in Bragaglia A., Davies M., Sills A., Vesperini E., eds, Proc. IAU Symp. 351, Star Clusters: From the Milky Way to the Early Universe. Cambridge Univ. Press, Cambridge, p. 13
Smith L. J., Bajaj V., Ryon J., Sabbi E., 2020, ApJ, 896, 84
Spengler C. et al., 2017, ApJ, 849, 55
Stiavelli M., Miller B. W., Ferguson H. C., Mack J., Whitmore B. C., Lotz J. M., 2001, AJ, 121, 1385
Stone N. C., Küpper A. H. W., Ostriker J. P., 2017, MNRAS, 467, 4180
Su A. H., Salo H., Janz J., Venhola A., Peletier R. F., 2022, A&A, 664, A167
Taylor M. B., 2005, in Shopbell P., Britton M., Ebert R., eds, ASP Conf. Ser. Vol. 347, Astronomical Data Analysis Software and Systems XIV. Astron. Soc. Pac., San Francisco, p. 29
Thornton C. E., Barth A. J., Ho L. C., Rutledge R. E., Greene J. E., 2008, ApJ, 686, 892
Trujillo I., Erwin P., Asensio Ramos A., Graham A. W., 2004, AJ, 127, 1917
Turner M. L., Côté P., Ferrarese L., Jordán A., Blakeslee J. P., Mei S., Peng E. W., West M. J., 2012, ApJS, 203, 5
van der Walt S., Colbert S. C., Varoquaux G., 2011, Comput. Sci. Eng., 13, 22
Virtanen P. et al., 2020, Nat. Methods, 17, 261
Wehner E. H., Harris W. E., 2006, ApJ, 644, L17
Williams D. R. A. et al., 2022, MNRAS, 510, 4909
Williams D. R. A. et al., 2023, Proc. Sci., 428, 046
Willmer C. N. A., 2018, ApJS, 236, 47
Yang J. et al., 2023, MNRAS, 520, 5964
Zanatta E., Sánchez-Janssen R., Chies-Santos A. L., de Souza R. S., Blakeslee J. P., 2021, MNRAS, 508, 986

APPENDIX A

A1 2D Decomposition

Fig. A1 displays the *HST* images and the residual images from the 2D multicomponent decompositions for the dozen representative nucleated galaxies whose 1D profiles are shown in Fig. 1. The residual images are generated after subtracting the best-fitting IMFIT model images from the galaxies' *HST* images.

A2 Literature comparison

To identify the 100 nuclei in this work, we have decomposed the full extent of the *HST* stellar light distributions of the 173 (23 E, 42 S0, 102 S, and 6 Irr) galaxies (Table 1), and, when necessary, fitted galaxy components beyond our multicomponent, bulge+disc+nucleus model (Figs 1, A1 and see also Dullo et al. 2023b). Table A1 presents previous studies of nucleation in nearby ($D \lesssim 100$ Mpc) galaxies, the pertaining data, the adopted galaxy fitting method, and sample size. Given the common presence of structural components such as bars, discs, and rings in nearby galaxies, employing a multicomponent galaxy decomposition that extends beyond the traditional bulge+disc profiles is essential. It enables us to properly investigate the scaling relations between nuclei and host bulge properties and SMBH masses.

Previous studies which performed multicomponent decompositions for photometric and structural analysis of nuclei include Balcells et al. (2003, 2007), Turner et al. (2012), Spengler et al. (2017), Su et al. (2022), and Román et al. (2023). However, our study of nuclei in 35 early-type and 65 late-type galaxies with *HST*

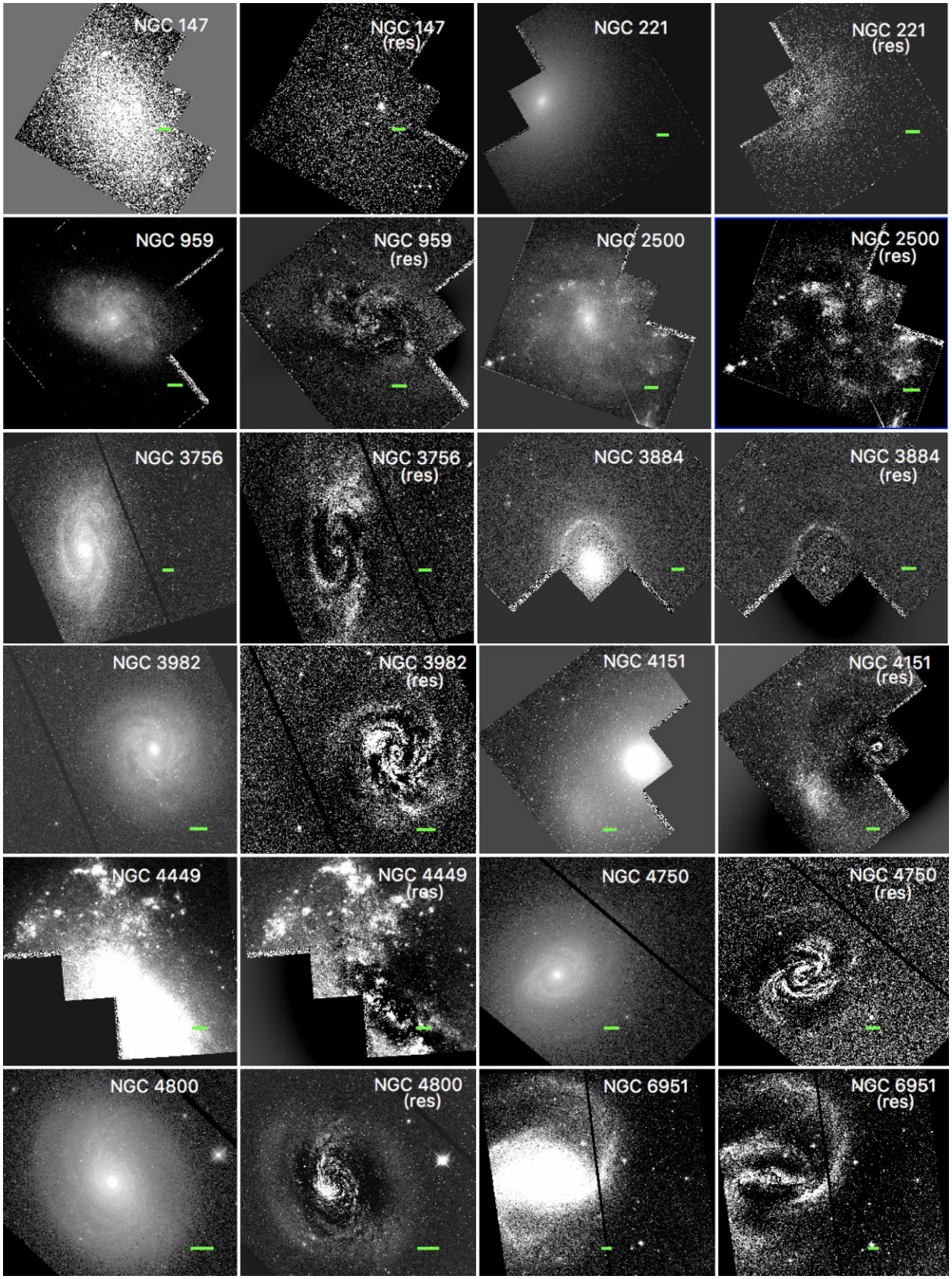

Figure A1. *HST* images and the corresponding residual images from our 2D multicomponent decompositions with IMFIT for the sample of 12 LeMMINGs galaxies shown in Fig. 1. The *HST* instruments and filters used for imaging the galaxies are as in Fig. 1 (see Section 2.3). The 2D fits have the same type and number of galaxy structural components as the corresponding 1D modelling (Fig. 1). We find good agreement between the 1D and 2D fits for the sample galaxies. The green scale bar is 10 arcsec in length.

Table A1. Comparison with previous studies of nucleation in nearby galaxies.

Study	Data used	Type	Method	$f_{\rm nuc}$	Full sample
This work	*HST*	ETs + LTs	multicompt (1D,2D)	58–67 per cent/core (10–20 per cent)	173
Su et al. (2022)	ground-based (seeing $\sim$ 1.1–1.2 arcsec)	dwarf + massive galaxies	multicompt (2D)	–	557
Poulain et al. (2021)	ground-based (seeing $\sim$ 0.5–1.6 arcsec)	dwarfs	PSFNuc + Sérsic(2D)	23 per cent	2210
Zanatta et al. (2021)	*HST*	low-mass, quiescent	PSFNuc + Sérsic(2D)	50 per cent	66
Hoyer et al. (2021)	compilation	local volume galaxies	SNuc + flatbg (2D)	–	601
Sánchez-Janssen et al. (2019)	ground-based (seeing $\sim$ 0.6 arcsec)	quiescent Virgo	SNuc + Sérsic (1D)	90 per cent	400
Georgiev & Böker (2014)	*HST*	Spirals	KingNuc(2D)	80 per cent	228
den Brok et al. (2014)	*HST*	ET dwarfs	PSFNuc + Sérsic	80 per cent	22
Turner et al. (2012)	*HST*	ETs	multicompt (1D,2D)	72 per cent	43
Balcells et al. (2007)	*HST*	S0–Sbc galaxies	multicompt (1D)	84 per cent	19
Côté et al. (2006)	*HST*	ETs Virgo	KingNuc + core-/Sérsic(1D)	(66–82 per cent)	100
Grant, Kuipers & Phillipps (2005)	ground-based (seeing $\sim$ 1.7–1.9 arcsec)	dEs	PSFNuc+Sérsic(1D + 2D)	61 per cent	181
Lauer et al. (2005)	*HST*	ETs	Nuc_excluded + Nuker(1D)	core (29 per cent)/power-law (60 per cent)	77
Graham & Guzmán (2003)	*HST*	dEs	PSFNuc + Sérsic(1D)	87 per cent	15
Carollo et al. (2002)	*HST*	Spirals	PSFNuc(1D)	65 per cent	69
Böker et al. (2002)	*HST*	LT spirals	Galaxy inc_Nuc, Nuker(1D)	77 per cent	77
Stiavelli et al. (2001)	*HST*	dEs	Nuc_excluded + Nuk/Ser(1D)	56 per cent	25
Ravindranath et al. (2001)	*HST*	ETs	PSFNuc + Nuker(1D,2D)	50 per cent	33
Carollo et al. (1998)	*HST*	Spirals	PSFNuc(1D)	50 per cent	75

Note. Ground-based and *HST* data have been used to study nucleation in early- and late-type (i.e. ET and LT) and quiescent galaxies. Previous studies in the literature which performed multicomponent decompositions for photometric and structural analysis of nuclei include e.g. Su et al. (2022). Several studies fitted the nuclei with a PSF model (e.g. Poulain et al. 2021), whereas others fitted a Sérsic model or a King profile (King 1962, 1966), see Côté et al. (2006). Stiavelli et al. (2001) and Lauer et al. (2005) fit the surface brightness profiles of their galaxies by excluding the nuclei. Böker et al. (2002) fitted the light profiles of their late-type spiral galaxies with a Nuker (nucleus+bulge) model. See Section A2 for further details.

Table A2. Global and central properties for our sample of 100 nucleated galaxies.

Galaxy	Type	D	Class	M_V (bulge)	M_V (gal)	$\log M_*$ (bulge)	$\log M_*$ (gal)	$M_{V,nuc}$	$\log M_{*,nuc}$	$R_{e,nuc}$	$R_{e,nuc}$ (1D/2D)	$\mu_{0,nuc}(\mu_{e,nuc})$ (1D/2D)	$\log L_{R,core}$	Det	$\log L_X$	Det	Type
		(Mpc)		(mag)	(mag)	($M_\odot$)	($M_\odot$)	(mag)	($M_\odot$)	(arcsec)	(pc)		(erg s^{-1})	(radio)	(erg s^{-1})	(X-ray)	(nuclei)
(1)	(2)	(3)	(4)	(5)	(6)	(7)	(8)	(9)	(10)	(11)	(12)	(13)	(14)	(15)	(16)	(17)	(18)
I0239	SAB	9.9	HII	–16.82	–18.80	9.1	9.8	–9.60	6.2	0.09	4.4/4.7	16.34/16.04	<35.0	N	<38.2	N	NSC
I0356	SA	11.7	HII	–16.63	–19.03	10.6	11.5	–9.10	7.6	0.02	0.8/1.3	11.73/11.77	35.5	Y	–	–	NSC
I0520	SAB	50.9	L	–20.74	–22.62	10.7	11.5	–15.48	8.6	0.10	23.5/27.8	15.31/15.09	<36.1	N	–	–	HYB
N0147	E5pec	0.8[k]	ALG	–15.76	–15.76	9.1	9.1	–6.04	5.2	1.43	5.7/5.2	(20.04/19.64)	<32.4	N	–	–	NSC
N0205	E5pec	0.8[k]	ALG	–18.22	–18.22	9.5	9.5	–9.80	6.2	0.36	1.5/1.3	(15.87/15.70)	<32.4	N	<35.8	N	NSC
N0221	E2	0.8[k]	ALG	–15.52	–16.48	8.6	9.0	–12.17	7.3	0.9	3.6/4.6	(13.10/13.13)	<32.3	N	<35.5	N	NSC
N0266	SB	62.9	L	–22.93	–23.36	11.8	12.0	–14.36	8.4	0.08	24.5/21.9	16.07/15.54	36.9	Y	40.9	Y	HYB
N0278	SAB	5.3	H	–16.04	–17.65	8.8	9.5	–10.82	6.7	0.07	1.7/1.9	12.66/12.42	34.8	Y	38.1	Y	NSC
N0404	E	3.1[k]	L	–17.39	–17.40	9.3	9.3	–12.06	7.2	0.30	4.2/5.0	13.53/13.38	<33.3	N	37.3	Y	HYB
N0959	Sdm?	5.4	HII	–14.68	–16.12	8.1	8.7	–10.38	6.4	0.16	4.0/3.8	15.59/15.08	<34.7	N	<38.0	N	NSC
N1058	SA	4.5	L	–13.36	–16.34	7.4	8.6	–12.53	7.0	0.87	19.0/14.0	(14.85/14.67)	<34.4	N	38.4	Y	HYB
N1161	S0	25.6	L/RL	–22.08	–22.25	11.4	11.5	–17.55	9.6	0.57	69.3/63.4	(17.21/16.93)	36.6	Y	40.0	Y	HYB
N1275	cDpec	73.9	L/RL	–23.50	–23.77	11.5	11.6	–17.77	9.2	0.08	27.7/31.8	12.86/12.78	41.0	Y	42.4	Y	HYB
N2273	SB	26.9	S	–20.74	–21.27	10.7	10.9	–15.37	8.6	0.26	33.3/38.0	15.39/15.67	36.6	Y	40.9	Y	HYB
N2342	Spec	78.6	HII	–19.78	–21.52	10.0	10.7	–16.54	8.7	0.13	46.9/78.0	15.59/15.34	36.5	Y	–	–	NSC
N2500	SB	9.0	HII	–14.39	–18.09	7.8	9.3	–11.21	6.6	0.09	3.9/3.6	(15.84/15.53)	<34.7	N	38.4	Y	NSC
N2549	SA0	16.6	ALG	–21.07	–21.74	10.9	11.2	–14.70	8.4	0.10	7.7/8.7	13.00/13.93	<35.3	N	39.5	Y	NSC
N2634	E1?	33.0	ALG	–19.68	–20.53	10.2	10.5	–14.23	8.0	0.10	15.9/14.8	14.31/14.35	35.8	Y	<39.6	N	NSC
N2655	SAB0	20.3	L/RL	–21.08	–21.72	11.0	11.2	–17.28	9.4	0.60	60.7/89.0	15.18/15.18	37.6	Y	–	–	HYB
N2681	SAB0	12.1	L	–19.0	–20.22	9.9	10.3	–15.2	8.3	0.19	11.0/9.2	11.74/11.54	35.5	Y	39.2	Y	HYB
N2685	SB0	14.4	L	–18.48	–19.88	10.1	10.6	–12.71	7.8	0.10	7.3/13.0	13.96/13.73	<34.8	N	–	–	HYB
N2748	SAbc	21.6	HII	–18.47	–21.18	9.7	10.8	–10.36	6.5	0.02	2.1/2.9	8.71/8.72	<35.4	N	38.4	Y	NSC
N2768	E6?	21.6	L/RL	–21.09	–21.27	11.4	11.5	–13.84	8.5	0.32	31.9/29.8	14.37/14.41	37.1	Y	39.8	Y	HYB
N2782	SAB	39.7	HII	–20.38	–21.51	10.5	10.9	–15.05	8.3	0.15	27.7/40.2	14.62/14.51	36.8	Y	40.8	Y	NSC
N2787	SB0	11.0	L	–18.08	–19.34	10.3	10.8	–12.62	8.1	0.09	5.0/7.4	12.99/12.78	36.3	Y	39.4	Y	HYB
N2859	SB0	27.8	L	–20.15	–20.88	11.1	11.4	–11.89	7.8	0.02	1.0/3.0	9.58/9.54	<35.3	N	–	–	HYB
N2903	SAB	12.1	HII	–15.04	–22.03	8.2	11.0	–11.98	7.0	0.05	3.1/4.9	13.65/13.39	<34.3	N	38.7	Y	NSC
N2950	SB0	20.9	ALG	–19.57	–20.46	10.8	11.1	–15.01	8.9	0.27	26.5/23.6	13.91/13.58	<35.5	N	39.3	Y	NSC
N2985	SA	19.8	L	–20.70	–21.13	10.8	11.0	–13.20	7.8	0.05	4.9/5.6	12.75/12.68	35.8	Y	39.8	Y	HYB
N3073	SAB0	19.1	HII	–18.14	–18.70	9.7	9.9	–9.73	6.3	0.04	3.9/1.0	8.13/8.14	<35.3	N	<38.4	N	NSC
N3077[†]	I0pec	1.4	HII	–	–16.24	–	9.0	–8.66	6.0	0.36	2.5/2.7	15.13/15.33	33.3	Y	37.6	Y	NSC
N3079	SB	18.3	L	–20.34	–22.33	10.2	11.0	–14.38	7.8	0.02	1.2/7.2	(18.82/18.05)	37.3	Y	40.1	Y	HYB
N3185	SB	22.0	S	–19.16	–19.94	10.3	10.6	–13.98	8.2	0.20	20.5/23.1	15.33/14.92	<35.2	N	39.9	Y	HYB
N3190	SA	21.8	L	–19.42	–21.79	10.8	11.7	–8.82	7.5	0.27	29.3/40.2	(18.69/19.34)	<35.3	N	40.3	Y	HYB
N3193	E2	24.3	L	–21.79	–21.93	11.4	11.4	–14.40	8.4	0.54	63.5/61.3	17.59/17.47	<35.2	N	39.6	Y	HYB
N3198	SB	12.6	HII	–20.74	–21.51	10.5	10.8	–12.98	7.4	0.21	12.5/20.9	12.55/12.26	35.0	Y	38.7	Y	NSC
N3245	SA0	22.3	HII	–20.74	–21.39	10.6	10.8	–13.50	7.7	0.04	4.3/6.8	12.20/12.23	35.7	Y	39.7	Y	NSC
N3319	SB	14.1	L	–19.44	–20.56	9.5	9.9	–12.85	6.9	0.13	8.9/8.3	15.83/15.77	<34.8	N	39.3	Y	HYB

Table A2 – *continued*

Galaxy	Type	D	Class	M_V (bulge)	M_V (gal)	$\log M_*$ (bulge)	$\log M_*$ (gal)	$M_{V,nuc}$	$\log M_{*,nuc}$	$R_{e,nuc}$	$R_{e,nuc}$ (1D/2D)	$\mu_{0,nuc}(\mu_{e,nuc})$ (1D/2D)	$\log L_{R,core}$	Det	$\log L_X$	Det	Type
		(Mpc)		(mag)	(mag)	($M_\odot$)	($M_\odot$)	(mag)	($M_\odot$)	(arcsec)	(pc)		(erg s^{-1})	(radio)	(erg s^{-1})	(X-ray)	(nuclei)
(1)	(2)	(3)	(4)	(5)	(6)	(7)	(8)	(9)	(10)	(11)	(12)	(13)	(14)	(15)	(16)	(17)	(18)
N3344	SAB	12.3	HII	–17.83	–20.82	9.3	10.5	–13.19	7.4	0.18	11.3/12.7	14.35/14.09	<34.1	N	38.6	Y	NSC
N3414	S0	24.4	L	–20.59	–20.77	11.3	11.4	–13.28	8.4	0.23	28.0/21.8	15.56/15.09	36.2	Y	40.6	Y	HYB
N3486	SAB	14.1	S	–18.58	–20.27	9.3	10.0	–13.75	7.4	0.15	9.9/13.5	13.75/13.84	<34.3	N	<37.5	N	HYB
N3504	SAB	26.2	HII	–20.43	–20.90	10.6	10.8	–15.36	8.6	0.26	32.1/46.9	12.66/12.53	37.3	Y	–	–	NSC
N3516	SB0	37.5	S	–21.01	–22.36	11.1	11.6	–16.80	9.4	0.19	35.7/40.4	12.94/12.78	36.8	Y	42.5	Y	HYB
N3610	E5?	25.6	ALG	–20.79	–20.88	10.6	10.6	–15.70	8.5	0.33	42.5/41.3	(13.29/13.28)	<35.6	N	39.6	Y	NSC
Error	–	–	–	0.30	0.33	0.15 dex	0.17 dex	0.35	0.24 dex	15 per cent	15 per cent	0.32	1 dex	–	1 dex	–	–
N3631	SA	19.2	HII	–20.13	–20.33	10.2	10.2	–13.24	7.4	0.24	22.1/35.2	16.45/15.97	<35.2	N	39.5	Y	NSC
N3718	SB	16.9	L/RL	–19.62	–20.15	10.5	10.7	–13.01	7.9	0.09	7.3/8.5	13.37/13.27	36.8	Y	41.3	Y	HYB
N3729	SB	17.8	HII	–16.22	–18.86	8.9	9.9	–12.89	7.6	0.25	21.5/9.1	16.12/16.08	35.8	Y	39.8	Y	NSC
N3756	SAB	21.4	HII	–17.81	–20.57	9.3	10.4	–12.79	7.2	0.06	5.5/5.3	14.20/14.02	<35.3	N	<38.5	N	NSC
N3884	SA0	107.0	L	–21.91	–23.12	11.6	12.0	–16.74	9.5	0.14	71.0/87.5	16.38/16.31	37.8	Y	42.1	Y	HYB
N3898	SA	19.2	L	–20.25	–20.59	11.0	11.1	–14.71	8.8	0.38	34.4/52.8	14.46/14.77	35.8	Y	39.4	Y	HYB
N3949	SA	14.5	HII	–19.92	–20.43	9.6	9.8	–13.49	7.1	0.08	5.5/7.7	14.32/14.23	<35.0	N	<39.1	N	NSC
N3982	SAB	18.3	S	–19.39	–20.77	8.7	9.2	–14.55	6.7	0.06	5.6/6.5	13.62/13.42	36.2	Y	39.2	Y	HYB
N3992	SB	17.6	L	–18.50	–21.12	9.8	10.9	–10.87	6.8	0.02	1.8/6.5	14.60/14.30	<35.1	N	39.0	Y	HYB
N3998	SA0	17.4	L/RL	–19.27	–20.04	10.9	11.2	–14.16	8.8	0.12	9.7/11.6	(12.67/12.74)	38.0	Y	42.0	Y	HYB
N4026	S0	16.9	L	–22.38	–23.12	11.3	11.6	–15.80	8.7	0.03	2.5/3.2	10.56/10.53	<35.1	N	38.9	Y	HYB
N4036	S0	21.7	L	–19.23	–21.45	10.5	11.4	–15.23	8.9	0.39	40.6/31.5	(15.87/16.14)	36.0	Y	40.4	Y	HYB
N4041	SA	19.5	HII	–19.32	–20.14	9.9	10.2	–13.54	7.6	0.15	13.6/14.1	(15.42/15.53)	35.5	Y	39.4	Y	NSC
N4062	SA	14.9	HII	–15.35	–20.31	8.4	10.4	–13.48	7.6	0.7	50.5/55.1	18.54/18.55	<34.6	N	<38.0	N	NSC
N4125	E6pec	21.0	L	–21.14	–21.14	11.3	11.3	–14.39	8.6	0.68	68.5/78.1	15.63/15.63	<35.4	N	39.5	Y	HYB
N4143	SAB0	16.9	L	–20.45	–21.22	10.9	11.2	–13.82	8.3	0.08	6.7/5.3	14.32/14.33	36.1	Y	40.3	Y	HYB
N4150	SA0	7.1	L	–15.80	–17.76	9.0	9.8	–13.31	8.1	0.52	17.7/30.0	14.88/14.93	<34.6	N	<37.8	N	HYB
N4151	SAB	17.8	S	–19.22	–20.85	10.2	10.8	–17.62	9.5	0.1	8.8/12.4	9.43/9.46	37.8	Y	42.4	Y	HYB
N4203	SAB0	19.5	L	–19.59	–20.44	10.9	11.2	–12.75	8.2	0.05	4.3/5.9	11.82/11.78	36.1	Y	40.5	Y	HYB
N4220	SA0	16.0	L	–18.26	–19.96	10.1	10.7	–13.08	8.0	0.83	63.5/65.1	(18.03/17.93)	35.2	Y	39.2	Y	HYB
N4245	SB0	16.7	HII	–19.28	–20.21	10.2	10.6	–12.81	7.7	0.18	14.6/12.0	(17.08/16.30)	<34.6	N	<38.0	N	NSC
N4258	SAB	9.4	S	–20.03	–21.72	10.8	11.5	–14.00	8.4	0.15	6.7/6.2	(14.15/14.08)	34.9	Y	40.7	Y	HYB
N4274	SB	17.4	L	–17.93	–20.10	9.6	10.4	–12.06	7.2	0.29	24.7/44.1	(18.34/18.49)	<34.6	N	<40.1	N	HYB
N4278	E1-2	15.6	L/RL	–20.91	–20.91	11.0	11.0	–11.57	7.2	0.08	5.0/4.8	13.32/13.00	37.6	Y	39.7	Y	HYB
N4314	SB	17.8	L	–19.74	–20.69	10.8	11.1	–13.20	8.1	0.22	18.7/25.7	14.73/14.81	<34.7	N	38.4	Y	HYB
N4414	SA	14.2	L	–19.14	–20.11	10.4	10.8	–10.98	7.1	0.06	3.9/6.3	13.47/13.58	<34.7	N	38.7	Y	HYB
N4449	IBm	6.1	HII	–16.61	–20.10	8.4	9.8	–13.21	7.0	0.24	6.7/8.3	14.46/14.43	<33.6	N	36.9	Y	NSC
N4559	SAB	15.6	HII	–16.16	–19.64	8.1	9.5	–14.25	7.3	0.1	6.3/7.0	13.87/13.85	<34.5	N	39.0	Y	NSC
N4565	SA	21.8	S	–21.70	–23.62	11.2	11.9	–9.86	6.4	0.05	4.8/3.9	16.81/16.85	35.2	Y	39.7	Y	HYB
N4648	E3	21.0	ALG	–18.66	–19.58	10.0	10.4	–11.04	7.0	0.04	4.0/5.5	13.13/12.90	<35.5	N	39.0	Y	NSC
N4656†	SBm	13.0	HII	–	–21.48	–	9.8	–10.88	5.6	0.54	34.0/42.3	(21.44/21.67)	<34.3	N	–	–	NSC
N4736	SA	7.6	L	–19.78	–21.35	10.5	11.1	–15.33	8.7	0.1	3.8/16.8	12.57/12.59	34.8	Y	39.5	Y	HYB
N4750	SA	24.1	L	–19.57	–20.89	10.2	10.8	–14.03	8.0	0.14	15.9/15.3	14.23/14.16	35.8	Y	40.4	Y	HYB
N4800	SA	15.6	HII	–19.24	–19.41	10.4	10.4	–12.37	7.6	0.08	5.9/6.6	13.53/13.54	<34.9	N	38.8	Y	NSC

Table A2 – *continued*

Galaxy	Type	D	Class	M_V (bulge)	M_V (gal)	$\log M_*$ (bulge)	$\log M_*$ (gal)	$M_{V,nuc}$	$\log M_{*,nuc}$	$R_{e,nuc}$	$R_{e,nuc}$ (1D/2D)	$\mu_{0,nuc}(\mu_{e,nuc})$ (1D/2D)	$\log L_{R,core}$	Det	$\log L_X$	Det	Type
		(Mpc)		(mag)	(mag)	($M_\odot$)	($M_\odot$)	(mag)	($M_\odot$)	(arcsec)	(pc)		(erg s^{-1})	(radio)	(erg s^{-1})	(X-ray)	(nuclei)
(1)	(2)	(3)	(4)	(5)	(6)	(7)	(8)	(9)	(10)	(11)	(12)	(13)	(14)	(15)	(16)	(17)	(18)
N4826	SA	10.0	L	–19.63	–21.45	10.5	11.2	–14.96	8.6	0.36	17.2/9.6	13.35/13.38	33.9	Y	38.1	Y	HYB
N5005	SAB	16.8	L	–21.30	–21.47	11.0	11.1	–14.22	8.2	0.12	9.8/6.3	13.20/13.58	36.3	Y	39.2	Y	HYB
N5033	SA	15.8	L	–20.00	–22.31	9.9	10.8	–14.31	7.6	0.13	9.4/9.9	13.79/13.67	36.0	Y	38.6	Y	HYB
N5055	SA	9.9	L	–17.70	–21.56	9.5	11.1	–15.8	8.8	0.61	29.3/29.1	13.73/13.77	<34.4	N	39.5	Y	HYB
N5112†	SB	17.0	HII	–	–19.51	–	9.5	–11.15	6.2	0.23	19.0/19.6	17.99/18.11	<35.4	N	–	–	NSC
N5377	SB	28.0	L	–20.99	–21.78	11.2	11.5	–16.48	9.4	0.18	24.7/29.3	13.11/12.88	35.7	Y	39.6	Y	HYB
N5457	SAB	5.2	HII	–15.72	–17.42	8.3	9.0	–9.96	6.0	0.21	5.1/4.9	16.59/16.19	<34.3	N	39.7	Y	NSC
N5474	SA	5.7	HII	–16.04	–17.59	8.4	9.0	–8.95	5.5	0.25	6.7/8.0	18.06/18.04	<34.4	N	38.6	Y	NSC
N5548	SA0	77.6	S	–21.45	–22.31	10.8	11.1	–19.06	9.8	0.07	24.1/34.1	12.02/12.02	37.0	Y	43.2	Y	HYB
N5585	SAB	5.6	HII	–14.11	–17.20	7.4	8.6	–10.96	6.1	0.15	3.9/3.6	(16.73/16.18)	<34.5	N	<36.2	N	NSC
N5879	SA	12.0	L	–18.20	–20.29	9.4	10.2	–11.54	6.7	0.06	3.7/2.8	14.87/15.33	35.3	Y	38.5	Y	HYB
N5985	SAB	36.7	L	–21.22	–22.70	10.8	11.4	–14.49	8.1	0.11	19.5/18.9	16.10/16.05	35.8	Y	41.5	Y	HYB
N6207	SA	12.3	HII	–17.36	–20.20	8.8	9.9	–9.86	5.8	0.06	3.8/3.6	16.77/16.70	<35.2	N	–	–	NSC
N6217	SB	19.1	HII	–18.40	–19.85	9.5	10.1	–15.37	8.3	0.11	9.9/6.9	12.29/12.52	35.7	Y	–	–	NSC
N6340	SA0	16.6	L	–19.78	–20.20	10.7	10.9	–14.02	8.4	0.38	30.5/25.3	15.38/14.89	35.5	Y	–	–	HYB
N6412	SA	18.1	HII	–17.82	–19.35	9.0	9.6	–11.25	6.4	0.08	6.0/5.8	15.57/14.77	<35.4	N	–	–	NSC
N6503	SA	4.9	L	–13.75	–19.20	7.7	9.9	–10.56	6.4	0.04	1.0/0.6	12.76/12.83	<34.3	N	38.1	Y	HYB
N6946	SAB	5.0	HII	–16.38	–18.79	8.3	9.3	–14.64	7.6	0.91	21.8/29.8	(16.46/16.88)	34.4	Y	<39.2	N	NSC
N6951	SAB	18.2	L	–20.25	–21.51	10.3	10.8	–14.34	7.9	0.15	13.3/12.9	14.01/14.07	35.4	Y	–	–	HYB
N7217	SA	9.0	L	–19.55	–19.86	10.6	10.7	–14.15	8.5	0.77	33.2/32.5	(16.47/16.37)	35.1	Y	–	–	HYB
N7331	SA	7.0	L	–17.62	–19.29	10.3	10.9	–12.30	8.1	0.27	9.18/11.1	(14.47/14.33)	<35.0	N	39.8	Y	HYB
N7457	SA0	7.2	ALG	–16.84	–18.11	9.6	10.1	–11.72	7.5	0.05	1.75/2.2	11.85/11.74	<34.9	N	<38.3	N	NSC
Error	–	–	–	0.30	0.33	0.15 dex	0.17 dex	0.35	0.24 dex	15 per cent	15 per cent	0.32	1 dex	–	1 dex	–	–

Note. (1) galaxy name. Bulgeless galaxies are indicated by the superscript '†'. (2) morphological classification from RC3 (de Vaucouleurs et al. 1991). (3) distance (D) are primarily from the NASA/IPAC Extragalactic Database (NED; http://nedwww.ipac.caltech.edu), other source is Karachentsev et al. (2004, k). (4) optical spectral class from Baldi et al. (2021a): H II, L = LINER, S = Seyfert and ALG = Absorption Line Galaxy. Radio-loud galaxies (RL) are based on classifications by Dullo et al. (2023a). (5)–(6) V-band bulge and galaxy absolute magnitudes calculated by integrating the best-fitting Sérsic or core-Sérsic functions. The magnitudes are given in the Vega magnitude system. (7)–(8) logarithm of the stellar masses of the bulge and galaxy. (9) V-band absolute magnitude of the nucleus calculated by integrating the best-fitting Gaussian or Sérsic function. (10) logarithm of the stellar mass of the nucleus. (11) angular 1D major-axis effective (half-light) radius of the nucleus in arcseconds. (12) 1D and 2D, major-axis effective radii of the nucleus in pc. (13) central and effective surface brightnesses of the nuclei, $\mu_{0,nuc}$ and $\mu_{e,nuc}$, respectively. $\mu_{0,nuc}$ and $\mu_{e,nuc}$ are in units of mag arcsec^{-2} and values given inside a parenthesis '()' are $\mu_{e,nuc}$. The *HST* filters in which $\mu_{0,nuc}$ and $\mu_{e,nuc}$ are obtained are given in Dullo et al. (2023b). (14) logarithm of the e-MERLIN 1.5 GHz radio core luminosity ($L_{R,core}$). (15) radio detection of the galaxies based on Baldi et al. (2021a): 'Y = Yes' = detected; 'N = No' = undetected. (16) logarithm of the (0.3−10 keV) X-ray core luminosity (L_X). (17) X-ray detection of the galaxies are from Williams et al. (2022): 'Y = Yes' = detected; 'N = No' = undetected. (18) our classification of nuclei based on multiwavelength data: NSCs and hybrid nuclei (HYB).

Table A3. Excluded nuclei.

Galaxy	Type	D	Class	M_V (bulge)	M_V (gal)	$\log M_*$ (bulge)	$\log M_*$ (gal)	$M_{V,nuc}$	$\log M_{*,nuc}$	$R_{e,nuc}$	$R_{e,nuc}$	$\log L_{R,core}$	Det	$\log L_X$	Det
		(Mpc)		(mag)	(mag)	($M_\odot$)	($M_\odot$)	(mag)	($M_\odot$)	(arcsec)	(pc)	(erg s^{-1})	(radio)	(erg s^{-1})	(X-ray)
(1)	(2)	(3)	(4)	(5)	(6)	(7)	(8)	(9)	(10)	(11)	(12)	(13)	(14)	(15)	(16)
I2574[†]	SAB	2.1	HII	–	–19.87	–	9.5	–4.83	3.5	0.242	2.4	<33.7	N	< 36.55	N
N0841	SAB	62.2	L	–21.34	–22.23	10.3	10.6	–20.17	9.8	1.498	438.9	<36.2	N	–	–
N1023	SB0	6.2	ALG	–19.36	–19.94	10.9	11.1	–10.69	7.4	<0.1	–	<34.6	N	39.05	Y
N1961	SAB(rs	56.4	L	–22.96	–23.50	11.3	11.5	–16.93	8.9	0.300	79.9	37.2	Y	40.43	Y
N2403	SAB(s)cd	2.6	HII	–19.58	–20.45	9.5	9.8	–16.19	8.1	21.443	278.8	<34.0	N	38.58	Y
N2541	SA(s)cd	9.8	HII	–12.92	–19.15	6.9	9.4	–8.21	5.0	<0.1	–	<34.7	N	38.10	Y
N2639	(R)SA	50.3	L	–20.74	–21.97	11.2	11.7	–16.80	9.6	0.427	101.6	37.6	Y	41.05	Y
N2683	SA(rs)	9.1	L	–19.64	–21.51	10.5	11.3	–16.07	9.1	2.503	110.2	34.5	Y	39.39	Y
N2770	SA(s)c?	31.4	HII	–18.62	–22.46	9.2	10.7	–14.24	7.4	0.710	106.5	<35.5	N	<38.34	N
N2964	SAB(r)	22.9	HII	–17.30	–20.85	9.3	10.7	–17.04	9.2	0.823	90.5	36.0	Y	–	–
N3031	SA(s)a	0.7	L	–16.62	–17.63	9.5	9.9	–7.92	6.0	0.142	0.4	35.5	Y	39.21	Y
N3184	SAB(rs)cd	11.4	HII	–16.62	–20.24	8.7	10.2	–13.55	7.5	1.355	77.2	<34.6	N	38.47	Y
N3642	SA(r)	24.9	L	–18.86	–20.63	9.4	10.1	–13.20	7.2	<0.1	–	<35.6	N	40.19	Y
N3838	SA0a?	21.0	ALG	–18.69	–22.11	10.0	11.4	–13.01	7.7	<0.1	–	35.4	Y	39.29	Y
N3900	SA0	30.2	ALG	–20.83	–21.61	10.7	11.1	–14.00	8.0	<0.1	–	<35.6	N	–	–
N4102	SAB	14.7	HII	–18.30	–18.77	10.6	10.8	–16.33	9.8	1.443	102.5	35.9	Y	40.83	Y
N4138	SA0	16.0	L	–20.01	–20.58	10.6	10.8	–14.93	8.5	1.101	84.8	<35.3	N	41.21	Y
N4448	SB	13.5	HII	–18.89	–19.38	10.6	10.8	–9.23	6.7	<0.1	–	<34.5	N	<38.48	N
N5204	SA(s)	4.6	HII	–17.75	–18.31	8.7	8.9	–6.93	4.3	0.236	5.2	<34.1	N	<36.18	N
N5273	SA0	18.6	S	–18.86	–20.24	10.1	10.6	–13.73	8.0	<0.1	–	35.3	Y	40.96	Y
N5308	S0	30.1	ALG	–19.99	–21.08	10.8	11.3	–17.52	9.8	0.645	92.9	<35.8	N	41.43	Y
N5354	S0ed	39.8	L	–20.52	–21.34	10.9	11.2	–15.82	9.0	0.603	114.0	36.9	Y	40.10	Y
N5448	(R)SAB	31.1	L	–19.77	–23.39	9.5	10.9	–16.53	8.2	0.556	82.8	35.7	Y	39.36	Y
N6654	(R')SB0	25.0	ALG	–18.61	–20.19	10.5	11.1	–10.83	7.3	<0.1	–	<35.6	N	–	–
Error	–	–	–	0.30	0.33	0.15 dex	0.17 dex	0.35	0.24 dex	15 per cent	15 per cent	1 dex	–	1 dex	–

Note. Similar to Table A2, but here for sample of nucleated LeMMINGs galaxies excluded from our analyses. Of the 24 excluded nuclei, 13 nuclei were too large for a NSC (+AGN) with extended half-light radii of $R_{e,nuc} \gtrsim 80$ pc. In contrast, 9/24 nuclei have sizes $R_{e,nuc} < 1$ pc based on our decomposition, whereas the remaining 2/24 nuclei have low stellar masses of $M_{*,nuc} < 10^5 M_\odot$. For eight nuclei unresolved in the *HST* images, we report upper-limit angular $R_{e,nuc}$ values.

Table A4. Radio and X-ray scaling relations for nuclei obtained using censored ASURV and uncensored BCES bisector regressions.

Relation	ASURV fit	r_s/P-value	r_p/P-value	δ_{horiz}	Sample
	Censored analysis				
$L_{R,core} - M_{*,nuc}$	$\log\left(\frac{L_{R,core}}{erg\ s^{-1}}\right) = (1.25 \pm 0.22)\log\left(\frac{M_{*,nuc}}{5\times10^7 M_\odot}\right) + (34.60 \pm 0.88)$	–	–	–	100
$L_{R,core} - M_{V,nuc}$	$\log\left(\frac{L_{R,core}}{erg\ s^{-1}}\right) = (-0.53 \pm 0.17)\left(M_{V,nuc} + 13.2\right) + (34.66 \pm 0.76)$	–	–	–	100
$L_X - M_{*,nuc}$	$\log\left(\frac{L_X}{erg\ s^{-1}}\right) = (1.09 \pm 0.16)\log\left(\frac{M_{*,nuc}}{4\times10^7 M_\odot}\right) + (39.09 \pm 0.28)$	–	–	–	84
$L_X - M_{V,nuc}$	$\log\left(\frac{L_X}{erg\ s^{-1}}\right) = (-0.48 \pm 0.10)\left(M_{V,nuc} + 13.2\right) + (39.22 \pm 0.20)$	–	–	–	84
	Uncensored analysis				
Relation	BCES bisector fit	r_s/P-value	r_p/P-value	δ_{horiz} (dex)	Sample
$L_{R,core} - M_{*,nuc}$	$\log\left(\frac{L_{R,core}}{erg\ s^{-1}}\right) = (1.15 \pm 0.22)\log\left(\frac{M_{*,nuc}}{5\times10^7 M_\odot}\right) + (35.40 \pm 0.10)$	$0.60/6.7 \times 10^{-11}$	$0.59/1.5 \times 10^{-10}$	0.96	100
$L_{R,core} - M_{V,nuc}$	$\log\left(\frac{L_{R,core}}{erg\ s^{-1}}\right) = (-0.49 \pm 0.07)\left(M_{V,nuc} + 13.2\right) + (35.41 \pm 0.55)$	$-0.55/2.6 \times 10^{-9}$	$-0.60/1.2 \times 10^{-10}$	–	100
$L_X - M_{*,nuc}$	$\log\left(\frac{L_X}{erg\ s^{-1}}\right) = (1.36 \pm 0.16)\log\left(\frac{M_{*,nuc}}{4\times10^7 M_\odot}\right) + (39.16 \pm 0.60)$	$0.63/1.4 \times 10^{-10}$	$0.65/1.6 \times 10^{-11}$	0.83	84
$L_X - M_{V,nuc}$	$\log\left(\frac{L_X}{erg\ s^{-1}}\right) = (-0.66 \pm 0.07)\left(M_{V,nuc} + 13.2\right) + (39.30 \pm 0.28)$	$-0.53/2.06 \times 10^{-7}$	$-0.58/5.24 \times 10^{-9}$	–	84

Note. Radio and X-ray scaling relations are based on the full sample of nuclei, without separating NSCs and hybrid nuclei. 1.5 GHz radio core luminosity from *e*-MERLIN ($L_{R,core}$) and (0.3–10 keV) *Chandra* X-ray core luminosity (L_X) as a function of nucleus stellar mass ($M_{*,nuc}$) and nucleus absolute magnitude ($M_{V,nuc}$). We performed the censored linear regressions using ASURV to account for upper limits. We present our BCES bisector regression fits to the galaxy data, the Spearman and Pearson correlation coefficients (r_s and r_p, respectively), and the corresponding serendipitous correlation probabilities. The horizontal rms scatter in the log $M_{*,nuc}$ direction is denoted with δ_{horiz}.

is based on the most detailed decompositions for the largest sample of galaxies to date (see Table A1).

A common approach for describing the stellar light distribution in nucleated galaxies is to limit the fit to a two-component model that describes the nucleus and the underlying galaxy (e.g. Pechetti et al. 2020; Poulain et al. 2021; Zanatta et al. 2021; Hoyer et al. 2023). Several studies modelled nucleated dwarf galaxies using a PSF (i.e. Gaussian) nucleus + Sérsic bulge model (Graham & Guzmán 2003; Grant et al. 2005; den Brok et al. 2014; Poulain et al. 2021; Zanatta et al. 2021). Carollo et al. (1997) and Carollo et al. (1998) fitted the nuclei in spiral galaxies with a PSF model. To separate the nuclei, these latter studies described underlying galaxy light with Gaussian wings and also attempted modelling the galaxy light in 2D, which was then subtracted from the galaxy images. Ravindranath et al. (2001) performed PSF nucleus+Nuker bulge model fits to the *HST* images of their early-type galaxies. Stiavelli et al. (2001) and Lauer et al. (2005) excluded the nuclei and performed Nuker model (Lauer et al. 1995) fits to the host galaxy *HST* profiles. Stiavelli et al. (2001) also fitted $R^{1/4}$, exponential, and Sérsic models to the bugle profiles. Böker et al. (2002) fitted the light profiles of their late-type spiral galaxies with a Nuker (nucleus + bulge) model. We note that Carollo et al. (1998), Ravindranath et al. (2001), Stiavelli et al. (2001), Böker et al. (2002), Carollo et al. (2002), and Lauer et al. (2005) used inner 10 arcsec *HST* images or light profiles to model the stellar light distributions of their galaxies. Côté et al. (2006) fitted King models to the nuclei and Sérsic or core-Sérsic models to the bulges of their early-type galaxies.

Recently, Georgiev & Böker (2014) and Georgiev et al. (2016) identified the nuclei in their spiral galaxy sample through visual inspection of the galaxies' *HST* images. To derive effective radii and luminosities for the nuclei, they used the ISHAPE task in BAOLAB (Larsen 1999) and fitted King profiles (King 1962, 1966) to the nuclei, restricting the fitted radial range typical to 0.5 arcsec. Sánchez-Janssen et al. (2019) and Ferrarese et al. (2020) modelled the ground-based data of their nucleated galaxies using a Sérsic nucleus + Sérsic bulge model. Hoyer et al. (2021, 2023) fitted a Sérsic model to the nuclei and a flat background model to the underlying light distributions of their galaxies.

A3 Data tables

Table A2 presents central and global properties for our sample of 100 nucleated galaxies, which includes distance, morphological classification, plus luminosities, stellar masses, and effective radii of the nuclei. Additionally, the table provides bulge and galaxy magnitudes and stellar masses, as well as radio and X-ray core luminosities. Table A3 is similar to Table A2 but presents properties for our sample of 24 nucleated LeMMINGs galaxies excluded from our analysis. Of the 24 excluded nuclei, 13 nuclei, with extended half-light radii of $R_{e,nuc} \gtrsim 80$ pc, were too large for a NSC (+AGN). In contrast, 9/24 nuclei have sizes $R_{e,nuc} < 1$ pc based on our structural decomposition, whereas the remaining 2/24 nuclei have low stellar masses of $M_{*,nuc} < 10^5$ $M_\odot$.

A4 Additional relations for nuclei

Table A4 presents radio and X-ray scaling relations for nuclei derived by fitting censored linear regressions using ASURV to account for upper limits and to help illustrate the good agreement between our censored (ASURV) and uncensored (BCES bisector) regression fits. The radio and X-ray scaling relations here are derived from the full sample of nuclei, without making a distinction between NSCs and hybrid nuclei, whereas in Section 4, NSCs and hybrid nuclei were fitted separately.

[1]*Department of Physical Sciences, Embry-Riddle Aeronautical University, Daytona Beach, FL 32114, USA*
[2]*Departamento de Física de la Tierra y Astrofísica, Facultad de CC. Físicas, Universidad Complutense de Madrid, E-28040 Madrid, Spain*
[3]*Instituto de Astrofísica de Canarias, Vía Láctea S/N, E-38205 La Laguna, Tenerife, Spain*

[4]*Departamento de Astrofísica, Universidad de La Laguna, E-38206 La Laguna, Tenerife, Spain*
[5]*Istituto di Radioastronomia - INAF, Via P. Gobetti 101, I-40129 Bologna, Italy*
[6]*School of Physics and Astronomy, University of Southampton, Southampton SO17 1BJ, UK*
[7]*Jodrell Bank Centre for Astrophysics, School of Physics and Astronomy, The University of Manchester, Alan Turing Building, Oxford Road, Manchester M13 9PL, UK*
[8]*Astrophysics Group, Cavendish Laboratory, 19 J. J. Thomson Avenue, Cambridge CB3 0HE, UK*
[9]*Instituto de Física de Partículas y del Cosmos IPARCOS, Facultad de CC. Físicas, Universidad Complutense de Madrid, E-28040 Madrid, Spain*
[10]*Department of Space, Earth and Environment, Chalmers University of Technology, SE-412 96 Göteborg, Sweden*
[11]*Instituto de Astrofísica de Andalucía, IAA-CSIC, Glorieta de la Astronomía s/n, E-18008 Granada, Spain*
[12]*Jeremiah Horrocks Institute, University of Central Lancashire, Preston, Lancashire PR1 2HE, UK*
[13]*Department of Astronomy, University of Wisconsin-Madison, Madison, WI, 53706, USA*
[14]*Max-Planck-Institut für Radioastronomie, Auf dem Hügel 69, D-53121 Bonn, Germany*
[15]*Real Academia de Ciencias, C/ Valverde 22, E-28004 Madrid, Spain*
[16]*Department of Astronomy and Space Science, Technical University of Kenya, P.O. box 52428-00200 Nairobi, Kenya*
[17]*Inter-University Centre for Astronomy and Astrophysics (IUCAA), P.O., Post Bag 4, Ganeshkhind, Pune 411 007, India*
[18]*Center for Astro, Particle and Planetary Physics, New York University Abu Dhabi, PO Box 129188 Abu Dhabi, UAE*
[19]*School of Physics and Astronomy, University of Birmingham, Birmingham B15 2TT, UK*

This paper has been typeset from a TEX/LATEX file prepared by the author.